# Resolving allogenic forcings on shallow-marine sedimentary archives of the Taiwan Western Foreland Basin

AMY I. HSIEH*'†'‡ iD, ROMAIN VAUCHER§'¶ iD, JAMES A. MACEACHERN† iD,
CHRISTIAN ZEEDEN** iD, CHUQIAO HUANG† iD, ANDREW T. LIN††'‡‡ iD,
LUDVIG LÖWEMARK‡ iD and SHAHIN E. DASHTGARD† iD

*Institute of Earth Sciences, University of Lausanne, Lausanne, Switzerland (E-mail: hsiehiamy@gmail.com)*
†*Department of Earth Sciences, Simon Fraser University, Burnaby, Canada*
‡*Department of Geosciences, National Taiwan University, Taipei, Taiwan*
§*College of Science and Engineering, James Cook University, Townsville, QLD, Australia*
¶*Department of Earth Sciences, University of Geneva, Geneva, Switzerland*
**LIAG-Institute for Applied Geophysics, Hannover, Germany*
††*Department of Earth Sciences, National Central University, Taoyuan, Taiwan*
‡‡*Carbon Storage and Geothermal Research Center, National Central University, Taoyuan, Taiwan*

Associate Editor – Marc Aurell

**ABSTRACT**

An investigation of allogenic forcings on shallow-marine strata of the Miocene–Pliocene Kueichulin Formation, Taiwan Western Foreland Basin, reveals that shifts in palaeoenvironments were strongly controlled by: (1) orogenesis and basin subsidence, (2) precession-driven hydroclimate and (3) obliquity-driven atmospheric and ocean circulation. Shifts from a wave-dominated open shelf to a tide-dominated shallow-marine deltaic environment were controlled by basin subsidence and the uplift and erosion of Taiwan. Rapid deepening of the Western Foreland Basin (~5400 Ka) and low sedimentation rates contributed to the development of lower offshore to distal delta front environments with limited fluvial and storm influence. As the uplift and erosion of Taiwan accelerated after ~4920 Ka, sediment filled the basin, forming shallow-marine deltaic environments. The emergence of Taiwan also led to the shallowing and narrowing of the palaeo-Taiwan Strait, resulting in strengthened tidal currents. Sedimentation from Taiwan is dominantly driven by tropical cyclone precipitation with lesser monsoon contribution, which is driven by summer insolation that mainly responds to eccentricity-modulated precession. Therefore, tropical cyclone beds preserved in the strata correspond to periods of maximum precession amplitudes, with the most amalgamated expressions occurring during periods of sea-level minima. Enhanced seasonal variations in insolation during periods of high obliquity amplitude may lead to fluctuations in ocean-atmospheric circulation, resulting in increased variability in sedimentation, and by extension, shifts in depositional environments. This is preserved in the Kueichulin Formation in facies that reflect the strengthening of tidal currents during periods of high obliquity amplitudes. The findings establish high-sedimentation and high-accommodation shallow-marine basins as potential records for effectively disentangling the relative influence of allogenic forcings on sedimentary systems, which is essential for understanding the response of the Earth's surface to climate, sea-level fluctuations and tectonism in the geologic past.

## INTRODUCTION

The sedimentary rock record represents an important archive that can be used to interpret and reconstruct palaeoenvironmental change over geological timescales, such as changes in the frequency and intensity of extreme weather events related to climate change in the Earth's past (e.g. Prieur *et al.*, 2025). Changes in the sedimentary environment may be driven by both allogenic processes (i.e. extrinsic drivers such as sea-level fluctuations, tectonic uplift and subsidence and/or climate changes) and autogenic processes (i.e. intrinsic drivers such as channel abandonment and delta lobe switching). To varying degrees, allogenic and autogenic processes influence changes in the supply, dispersal and deposition of sediment, its erosion and, correspondingly, its preservation, all of which may be imprinted in the sedimentary record (e.g. Jervey, 1988; Schlager, 1993; Burgess & Prince, 2015). As a result, the ability to distinguish different allogenic and autogenic processes that control deposition is crucial for reconstructing sedimentary environments in the Earth's past (e.g. Castelltort *et al.*, 2017; Hajek & Straub, 2017; Vaucher *et al.*, 2024).

Herein, we present a semi-quantitative analysis of facies preserved in shallow-marine strata of the late Miocene to Pliocene Kueichulin Formation in the Taiwan Western Foreland Basin (WFB; Fig. 1) to evaluate the combined effects of climate change at Milankovitch scales (≥20 kyrs) and tectonic forcing (>1000 kyrs) on the evolution of sedimentation processes and palaeoenvironments. Autogenic drivers are excluded from this study as they typically have timescales of less than 10 kyrs (e.g. Exner, 1925; Cazanacli *et al.*, 2002; Sun & Parker, 2005; Edmonds & Slingerland, 2007; Jerolmack & Mohrig, 2007; Jerolmack & Sadler, 2007; Kim & Paola, 2007; Jerolmack & Paola, 2010; Cojan & Gillot, 2022). Facies reflect discrete depositional processes operating in sedimentary environments and are based on both physical sedimentological characteristics (e.g. lithology, grain size, sedimentary structures, bedding contacts and accessory features) and biogenic sedimentary attributes (e.g. bioturbation intensity, bioturbation distributions and ichnological assemblages). Traditional indicators used to evaluate forcing on sedimentary environments (e.g. lithology, grain size, calculated sediment supply) are not unique to any single depositional environment and can reflect a variety of depositional processes. In contrast, facies are based on process interpretations that are reflective of depositional conditions within discrete sedimentary environments, and hence, serve as more robust indicators of environmental change.

In contrast to traditional cyclostratigraphic studies, which typically focus on strata that exhibit *visually* apparent cyclic patterns in environments of rather stable sedimentation rates, our study adopts a novel approach by evaluating sedimentary successions that do not exhibit obvious visual signs of cyclicity (i.e. rhythmically interbedded mudstone and sandstone). However, sedimentary attributes within the succession, such as gamma-ray signatures, reveal quasi-cyclic variations at Milankovitch frequency bands that are not readily discernible through visual inspection (Hsieh *et al.*, 2023a). Rather than assuming or pre-selecting cyclicity based on visual inspection, this study seeks to evaluate the relative influence of climate cycles versus tectonism on sedimentary facies. We suggest that this approach minimizes the risk of circular reasoning that may arise from focusing solely on already cyclic strata and ascribing climate as the main driver of cyclicity, thus offering a more robust framework for understanding climate-related versus tectonic-related controls on sedimentary records.

The ability to resolve allogenic controls on sedimentary processes from the stratigraphic record can complement and constrain modelled projections of extreme weather-event intensity. Previous reconstructions of forcings on sedimentary systems have generally considered grain size, lithology and sediment supply/provenance as the dominant indicators of environmental change (e.g. Whittaker *et al.*, 2011; Armitage *et al.*, 2013; Romans *et al.*, 2016; Li *et al.*, 2018; Sharman *et al.*, 2019). However, while single-variable proxies (e.g. grain size, lithology, sediment supply) are easily measured and quantified (Armitage *et al.*, 2013; Romans *et al.*, 2016), they
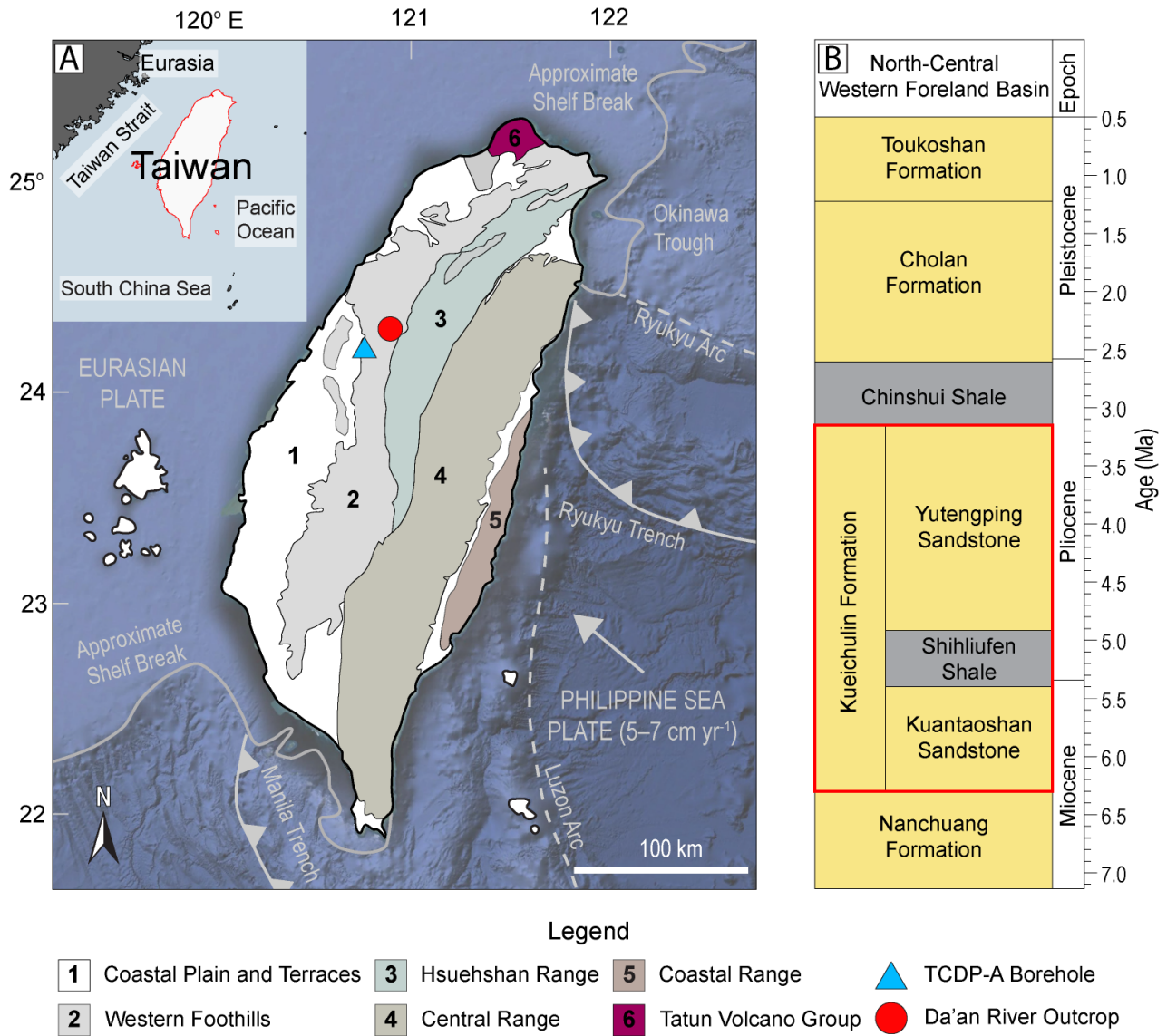
**Fig. 1.** (A) Simplified geological map of Taiwan showing the main geological provinces (data from Lin *et al.*, 2003; Simoes & Avouac, 2006; Lin & Chen, 2016) and locations of the Da'an River outcrop (120.91062° E, 24.29479° N) and the Taiwan Chelungpu-fault Drilling Project-A (TCDP-A; 120.73916° E, 24.20083° N) borehole of the Kueichulin Formation. The inset map shows the geographical location of Taiwan (background image source: Google Earth). (B) Geochronology of sedimentary strata in north-central parts of the WFB of Taiwan (after Teng *et al.*, 1991; Chen, 2016; Hsieh *et al.*, 2023a). Yellow denotes that the main lithology is sandstone, and grey indicates shale.

are not reflective of distinct sedimentary environments or of sedimentary processes. Shifts in sediment provenance, for example, may cause changes in the sedimentary record, but are difficult to constrain, especially in marine environments and in tectonically active regions wherein sediment mixing is pronounced and sediment sources change through time (e.g. Hsieh *et al.*, 2024). As well, reconstructions of sedimentary systems tend to focus on the importance of either climate-driven or climate-independent drivers, but the combined effects of these forcings have yet to be resolved effectively.

Finally, palaeoclimate reconstructions also traditionally focus on using proxies from

low-energy depositional settings, such as deep-marine and lacustrine environments, because they are regarded as being associated with relatively continuous sediment deposition over long time scales, resulting in the preservation of a relatively 'complete' climate record (Sadler, 1981). Shallow-marine settings are more susceptible to sediment reworking, which may remove or 'shred' environmental records (Jerolmack & Paola, 2010; Lazarus et al., 2019). However, in high-sedimentation and high-accommodation basins, the effects of such 'shredding' in shallow-marine settings may be diminished, resulting in the preservation of a high-resolution, direct record of environmental change at Milankovitch-scales or longer (i.e. >20-kyr resolution; e.g. Marshall et al., 2017; Grant et al., 2019; Vaucher et al., 2021; Hsieh et al., 2023a; Vaucher et al., 2023b; Vaucher et al., 2024).

## STUDY AREA

### Geological setting

The Taiwan Orogen (Fig. 1A) formed through the oblique collision of the Luzon Arc on the Philippine Sea Plate and the Eurasian Plate (e.g. Suppe, 1981, 1984; Lin et al., 2003). This collision began in the late Miocene and triggered lithospheric thickening and flexure that subsequently formed the WFB (e.g. Lin & Watts, 2002). Before Taiwan emerged from the Pacific Ocean, sedimentation in the WFB (i.e. the palaeo-Taiwan Strait) was derived primarily from Eurasia (Chen et al., 2019; Garzanti et al., 2021). However, at the Miocene–Pliocene transition (~5.3 Ma), a shift in the sediment source occurred, and the emergent Taiwan Orogen became the major source of sediment to the basin (Dashtgard et al., 2021; Hsieh et al., 2023b).

Taiwan is divided into five main geological realms from west to east: Coastal Plain, Western Foothills, Hsuehshan Range, Central Range and Coastal Range (Fig. 1A; Lin & Chen, 2016). The Western Foothills (Fig. 1A) are a fold-and-thrust belt that exposes sedimentary units ranging from the Oligocene to Recent. In the northern part of the Western Foothills, the Kueichulin Formation (late Miocene to early Pliocene), Chinshui Shale (late Pliocene), Cholan Formation (early to middle Pleistocene) and Toukoshan Formation (middle to late Pleistocene). Collectively, these strata form the sedimentary fill of the WFB (Fig. 1B;

Teng, 1990; Nagel et al., 2013). These formations reflect deposition in shallow-marine (nearshore to offshore) environments along the margin of the palaeo-Taiwan Strait and were influenced by tidal and fluvial processes with subordinate wave influence (Castelltort et al., 2011; Nagel et al., 2013; Pan et al., 2015; Dashtgard et al., 2020; Vaucher et al., 2023a). The ages of strata are well-constrained through a combination of magnetostratigraphy, biostratigraphy and cyclostratigraphy (Chen, 1977; Horng & Shea, 2007; Nagel et al., 2013; Pan et al., 2015; Vaucher et al., 2021, 2023b; Hsieh et al., 2023a).

The Kueichulin Formation (Fig. 1B), which is the focus of this study, records the emergence of Taiwan and encompasses (from base to top): the Kuantaoshan Sandstone (predating the emergence of Taiwan), Shihliufen Shale (onset of Taiwan's emergence) and Yutengping Sandstone (early-emergent Taiwan) (Fig. 1B; Nagel et al., 2013; Dashtgard et al., 2020; Dashtgard et al., 2021; Hsieh et al., 2023b).

### Environmental background

The continued rapid uplift and active tectonism of Taiwan results in frequent earthquakes and mass-wasting events that liberate an abundant supply of sediment from the orogen (Dadson et al., 2003; Milliman & Kao, 2005; Milliman et al., 2007; Chen et al., 2018). This sediment is subsequently delivered to adjacent seas during periods of high precipitation associated with tropical cyclones and the East Asian Summer Monsoon (Dadson et al., 2003; Hilton et al., 2010; Kao et al., 2014; Lin et al., 2020). Taiwan is located at the terminus of high-intensity (i.e. category 4 to 5 on the Saffir-Simpson Hurricane Intensity Scale) tropical cyclones in the western Pacific Ocean (Milliman et al., 2017). Over the last 35 years, on average, 3.5 TCs pass over Taiwan or within 50 km of the coastline per year (Dashtgard et al., 2020). Super-TCs (i.e. category 4 to 5 on the Saffir-Simpson Hurricane Intensity Scale; Kelman, 2013) impact Taiwan approximately once every 4 years. Tropical cyclones account for 47.5% of annual rainfall in Taiwan (Chen et al., 2010). Tropical cyclone precipitation delivers high volumes of sediment discharged through rivers (Dadson et al., 2003, 2004; Milliman & Kao, 2005; Chien & Kuo, 2011; Chen et al., 2018; Dashtgard et al., 2021; Hsieh et al., 2023b). Over 75% of the sediment delivered from Taiwan to the surrounding seas occurs during tropical cyclones (Milliman et al., 2007;

Kao & Milliman, 2008; Chen *et al.*, 2018), and this is amplified if a tropical cyclone interacts with the East Asian Summer Monsoon season (Chien & Kuo, 2011; Wu *et al.*, 2011; Lee *et al.*, 2015; Vaucher *et al.*, 2021).

A substantial volume of terrestrially sourced sediment delivered by rivers during tropical cyclone-induced floods is supplied to the shelf through hyperpycnal and hypopycnal flows (e.g. Milliman & Kao, 2005; Milliman *et al.*, 2007). In the modern-day Taiwan Strait, tropical cyclones not only provide precipitation that serves to deliver sediment from its steep-gradient rivers, but storm waves also rework the sediment deposited in shallow-marine environments (i.e. storm flood and river flood; Collins *et al.*, 2017; Lin & Bhattacharya, 2021; MacEachern & Bann, 2023; Vaucher *et al.*, 2023a). The relatively warmer temperatures of the late Miocene and Pliocene resulted in increased fluctuations in sea-surface temperature and ice volume, which resulted in more frequent and more intense tropical cyclones than occur in the modern day (Fedorov *et al.*, 2010; Coumou & Rahmstorf, 2012; Yan *et al.*, 2016; Kossin *et al.*, 2020).

## MATERIALS AND METHODS

This study is based on sedimentary data from one outcrop and one cored section with an accompanying gamma-ray profile. Both intervals extend through the late Miocene to late Pliocene-aged Kueichulin Formation in west-central Taiwan. The 429 m thick outcrop section along the Da'an River in central Taiwan (Fig. 1A) extends from the upper Kuantaoshan Sandstone through the majority of the Yutengping Sandstone (Dashtgard *et al.*, 2020; Hsieh *et al.*, 2023b). The 407 m long core was acquired through the Yutengping Sandstone as part of the Taiwan Chelungpu-fault Drilling Project-A (TCDP-A, Fig. 1A; Lin *et al.*, 2007).

### Core and outcrop data

Sedimentary facies are defined for the Kueichulin Formation based on descriptions of the Da'an River outcrop (Dashtgard *et al.*, 2020; Hsieh *et al.*, 2023b) and the TCDP-A core (this study), including lithology, grain size, sedimentary structures, bedding contacts, accessory features and ichnological descriptions (Table 1; Figs. 2 and 3). Ichnological descriptions include trace-fossil identifications and bioturbation

index assessments (BI 0 to 6; Reineck, 1963; Taylor & Goldring, 1993). The disarticulated and broken condition of all body fossils found in the Kueichulin Formation precludes identification and use for age determination. The TCDP-A wellbore was drilled at a slight angle from vertical (Lin *et al.*, 2007). Through the Yutengping Sandstone, the bedding dips at ~30° (combination of structural dip and drill angle), and bed thicknesses are corrected accordingly.

Gamma-ray (GR) data from the TCDP-A wellbore are used as a proxy for lithology due to its high resolution (Lin *et al.*, 2007). In siliciclastic rocks, low GR values (<75 American Petroleum Institute (API) units) generally correspond to sandstone-dominated intervals, high GR values (>105 API) reflect mudstone-dominated intervals enriched in radiogenic minerals, and GR values between 75 and 105 API correspond to heterolithic units or muddy sandstone/sandy mudstone (Green & Fearon, 1940; Schlumberger, 1989).

### Time-series analysis

Time-series and astrochronological analyses of the Da'an River outcrop and the TCDP-A core are completed using the open-source software 'R' and the 'astrochron' package (Meyers, 2014; R Core Team, 2022) in both the depth and time domains. A cyclostratigraphic age model for the Kueichulin Formation was created by Hsieh *et al.* (2023a) by correlating gamma-ray data from the formation to an astronomically tuned, benthic foraminiferal, stable oxygen isotope ($\delta^{18}O$) record from the equatorial Atlantic Ocean (Wilkens *et al.*, 2017), where low gamma-ray values (i.e. sandstone-rich) are correlated to high $\delta^{18}O$, and vice versa. Prominent shifts in facies and their subcomponents (i.e. lithology, grain size and BI) in the depth and time domains are compared to orbital cycles (i.e. 405 kyr long eccentricity, 100 kyr short eccentricity, 41 kyr obliquity and 23 kyr precession) to evaluate orbital forcing on the sedimentary system. The magnetobiostratigraphic (Figs S1 and S2) and astronomically tuned (Figs 7 and 8) datasets are also compared to orbital indices calculated by Laskar *et al.* (2004) to assess the relationship between sedimentary facies and/or their characteristics and orbital forcing. Furthermore, the datasets are compared to global mean sea-level and the p-0.5 t curve that is not related to any specific latitude but is most similar to summer insolation received at ~65° latitude in the Northern Hemisphere (Lourens *et al.*, 1996).

**Table 1.** Sedimentary facies descriptions and process interpretations. Acronyms: [grain size] very fine-grained (vfg); fine-grained (fg), medium-grained (mg) | [sedimentary structures] hummocky cross stratification (HCS), soft-sediment deformation (SSD) | [ichnology] bioturbation index (BI); *Arenicolites* (Ar), *Asterosoma* (As), *Chondrites* (Ch), *Cylindrichnus* (Cy), *Diplocraterion* (Di), fugichnia (fu), *Macaronichnus* (Ma), *Ophiomorpha* (Op), *Palaeophycus* (Pa), *Phycosiphon* (Ph), *Planolites* (Pl), *Rosselia* (Ro), *Schaubcylindrichnus* (Sch), *Scolicia* (Sc), *Skolithos* (Sk), *Teichichnus* (Te) and *Thalassinoides* (Th).

| Facies | | | Sedimentology | | | | |
| No. | Name | Bed thicknesses | Grain size | Sedimentary structures | Ichnology | Fossils and accessories | Process and environmental interpretation |
|---|---|---|---|---|---|---|---|
| F1 | Bioturbated mudstone | 30 to 500 cm | Dominantly mud Minor vfg sand | Rare wavy-parallel to planar-parallel laminae of siltstone and sandstone Multiple coarsening-upward cycles | BI 3 to 5, less commonly 6, and locally 1 to 2 in laminated siltstone and sandstone Pl, Ro, Sk, Th | Bivalve shells, crab and gastropod fossils, and rare coal fragments | Suspension settling of mud under low-energy conditions Pervasive infaunal colonization and preservation of burrows resulting in poor preservation of sedimentary structures Rare coal fragments indicate minimal fluvial influence **Lower offshore environment** |
| F2a | Bioturbated sandy mudstone to muddy sandstone | 1 to 20 cm | Mud with lower vfg to lower fg sand | Rare planar to wavy parallel laminated sand in mudstone Rare HCS and SSD | BI 4 to 5, less commonly 6, and locally 0 to 2 in laminated sandstone beds Ar, As, Ch, Op, Pa, Ph, Pl, Sch, Sk, Th Rare Sc | Rich in *Ditrupa* in Kuantaoshan Sandstone Disarticulated bivalve shell fragments, rip-up clasts, rare coal fragments | Rarely preserved laminated/HCS sandstones are interpreted as tempestites Agglomerations of *Ditrupa* tubes and shell and coal fragments suggest deposition under high-energy currents **Upper offshore environment** |

**Table 1.**  (continued)

| Facies | | Sedimentology | | | | Fossils and accessories | Process and environmental interpretation |
|---|---|---|---|---|---|---|---|
| No. | Name | Bed thicknesses | Grain size | Sedimentary structures | Ichnology | | |
| F2b | Bioturbated sandy mudstone to muddy sandstone with laminated sandstone interbeds | 1 to 20 cm with sandstone interbeds ranging from ~5 to 10 cm | Mud and upper vfg to upper fg sand Locally, beds of lower mg sand | Sharp-based, planar parallel-laminated to cross-laminated sandstone and rare HCS sandstone capped by massive to wavy parallel laminated mudstone | BI 3 to 5, less commonly 6, and locally 0 to 2 in laminated sandstone beds Ar, As, Ch, Op, Pa, Ph, Pl, Ro, Sch, Sk, Te, Th Rare Di | Rare disarticulated bivalve shell fragments, crab and gastropod fossils, and coal fragments | Rarely preserved laminated/HCS sandstones are interpreted as tempestites Dark mudstone laminae and drapes and coal fragments record fluvial discharge/influence, likely from hypopycnal plumes during river floods **Distal delta front environment** |
| F3a | Heterolithic, lenticular-bedded to wavy-bedded mudstone and (silty) sandstone | ~70% mudstone and ~30% sandstone Mudstone beds ~5 to 10 cm and sandstones ~1 to 2 cm thick (up to 10 cm when amalgamated) | Mud with minor silt Lower vfg to lower fg sand in sandstone beds | Sharp-based, massive to planar parallel-laminated mudstone Rare local inverse grading interbedded with current ripple-laminated to wavy parallel-laminated sandstone Rare SSD Sandstone beds typically have sharp or erosive basal surfaces | Bioturbation largely confined to mudstone layers BI 1 to 3, less commonly 4 in mudstone beds BI 0 to 1 in laminated sandstone beds Ar, As, Ch, Op, Ph, Pl Rare? Pa, Ro, Sch | Rare rip-up clasts Disarticulated bivalve shell fragments Coal fragments | Fluctuating energy conditions and sediment load, with repeated waning of unidirectional to oscillatory flow, followed by low-energy conditions allowing for rapid mud deposition through suspension settling from hypopycnal plumes associated with river floods Low-abundance to moderate-abundance, moderate-diversity trace-fossil suite suggests the palaeo-environment was stressful for infauna, which is consistent with fluctuating energy conditions, sedimentary rates and/or chemical stresses **Delta-front deposition in a tidal strait environment** |

**Table 1.**  (continued)

| Facies | | Sedimentology | | | Ichnology | Fossils and accessories | Process and environmental interpretation |
|---|---|---|---|---|---|---|---|
| No. | Name | Bed thicknesses | Grain size | Sedimentary structures | | | |
| F3b | Heterolithic, wavy-bedded to flaser-bedded sandstone with mudstone | ~60% sandstone and ~40% mudstone Sandstone beds 5 to 10 cm with amalgamated sandstone beds up to 20 cm thick Mudstone beds ~1 to 2 cm | Lower vfg to upper fg sand and mud Up to lower mg sand (locally) in sandstone beds | Sharp-based, massive (structureless) to parallel-laminated and current-rippled sandstone Less common trough cross-stratification and low-angle planar tabular cross-bedding Massive to wavy parallel-laminated, sharp-based mudstone HCS is uncommon, and SSD beds are present locally | BI 0 to 2 Top-down burrows dominate Ar, As, Op, Ph, Pl, Ro, Th Rare Sch | Rare rip-up clasts Disarticulated bivalve shell fragments Coal fragments Rare carbonaceous laminae | Deposition under high-energy, unidirectional flow with high sediment load (probable hyperpycnal and hypopycnal discharge) Decreasing energy conditions permitted deposition of current-ripple laminated sandstone followed by suspension settling of mud as drapes over ripples, likely from hypopycnal discharge Paucity of bioturbation and diminution of trace fossils indicate stressed conditions consistent with intermittent periods of high-energy, rapid sedimentation rates, and/or chemical stresses **Delta-front deposition in a tidal strait environment with increased fluvial influence** |

**Table 1.** (continued)

| Facies | | Sedimentology | | | | | | Process and environmental |
| No. | Name | Bed thicknesses | Grain size | Sedimentary structures | Ichnology | Fossils and accessories | | interpretation |
|---|---|---|---|---|---|---|---|---|
| F4a | Massive (structureless) and low-angle planar cross-stratified to trough cross-stratified silty sandstone to sandstone | Sandstone beds 10 to 150 cm Mudstone drapes 1 to 5 cm | Upper vfg to upper fg sand with interstitial silt and minor clay | Sharp-based, massive (structureless) or trough cross-angle to low-angle planar tabular cross-stratified sandstone beds commonly truncate underlying strata Foresets dip in multiple directions Wave ripples (locally aggradational) common in sandstone beds towards the tops of beds Capped by organic-rich, apparently structureless to laminated, sharp-based mudstone | BI 0 to 1, locally up to BI 3 in muddier beds Primarily top-down burrows Dominated by Op Rare Cy, Ma | Plant debris throughout sandstone Rip-up clasts of mudstone and coal, typically at the bases of sandstone beds Beds rich in disarticulated bivalve shell fragments and shell hash common Mudstone beds locally made up of 100% carbonaceous debris | | Rapid deposition of sediment by current-generated processes near fluvial sources, forming both 2D and 3D dunes Aggradation of wave ripples represent deceleration of bottom currents and transition to oscillatory flow coupled with high sediment supply Sharp-based, massive to laminated mudstone beds are interpreted as fluid mud deposits from river flood-derived hypopycnal plumes Paucity of bioturbation indicates stressed conditions, consistent with intermittent periods of high-energy, rapid sedimentation, and/or chemical stresses **Delta-front environment** |

**Table 1.**  (continued)

| Facies | | Sedimentology | | | | Fossils and accessories | Process and environmental interpretation |
|---|---|---|---|---|---|---|---|
| No. | Name | Bed thicknesses | Grain size | Sedimentary structures | Ichnology | | |
| F4b | Planar parallel and hummocky cross-stratified sandstone | Sandstone beds 10 to 50 cm thick Mudstone drapes up to 1 cm | Lower fg to lower mg sand Minor interstitial clay | Sharp-based, amalgamated planar parallel laminated to hummocky cross-stratified sandstone Typically grades into current-rippled (locally aggradational) sandstone, capped by massive to wavy parallel laminated mudstone | BI 0 to 2, rarely 4 to 5 Primarily top-down burrows Dominated by Op Ch, Pl, Ro, and Th locally in mudstone beds Rare fu | Rip-up clasts of mudstone and coal commonly deposited at the base sandstone beds Plant debris and carbonaceous laminae are common | Deposition by tropical cyclone events under high-energy, oscillatory or combined flow conditions, coupled with an elevated sediment supply rich in terrestrial organic material Amalgamated laminated sandstone beds likely deposited by successive storm events that scoured into underlying storm beds Low bioturbation intensities, presence of escape structures, rip-up clasts, and organic debris are consistent with high depositional energy Mudstone beds are attributed to post-storm hypo-pycnal and hyperpycnal flows **Delta front environment** |
| F5 | Soft-sediment deformed beds | 10 to 200 cm | Lower vfg to lower fg sand | Deformed beds showing convolute bedding Primary stratification not preserved | BI 0 No primary burrowing preserved | | Liquefaction of water-saturated/unconsolidated sediment |

The astronomically tuned datasets are filtered using a Taner bandpass filter (Taner, 1992) at different periodicities to evaluate the individual effects of eccentricity, obliquity and precession forcing on facies patterns. This is done by applying low-cut-off and high-cut-off frequencies of 0.0125 and 0.007 cycle $kyr^{-1}$ for eccentricity; 0.03 and 0.021 cycle $kyr^{-1}$ for obliquity; and 0.06 and 0.04 cycle $kyr^{-1}$ for precession (Zeeden *et al.*, 2018). The amplitudes of eccentricity, obliquity or precession-frequency components are isolated using a Hilbert transform and compared to orbital indices (Figs S3 and S4; Laskar *et al.*, 2004).

## RESULTS

### Sedimentary facies

#### Bioturbated mudstone (facies 1)
*Description.* Facies 1 consists of bioturbated mudstone with rare wavy-laminated to planar parallel-laminated siltstone interbeds that show subtle coarsening-upward cycles (Fig. 4; Table 1). Bioturbation intensities are generally high (BI 3 to 5, less commonly 6). Mud-filled trace fossils are difficult to identify owing to a lack of lithologic contrast with the mudstone matrix. Readily identifiable ichnogenera include *Planolites*, *Rosselia*, *Skolithos* and *Thalassinoides*.

*Interpretation.* The physical and biogenic sedimentary features of Facies 1 suggest deposition in a lower offshore environment. In such settings, low-energy conditions allowed for suspension settling of mud and pervasive infaunal colonization (e.g. Milliman *et al.*, 2007). The presence of rare coal fragments indicates minimal fluvial influence. The uncommon storm-generated sedimentary structures (e.g. laminated siltstones) suggest these strata were deposited below fairweather wave base and close to but generally above storm wave base, in water depths >35 m (Dashtgard *et al.*, 2021) and above 100 m (Nagel *et al.*, 2013).

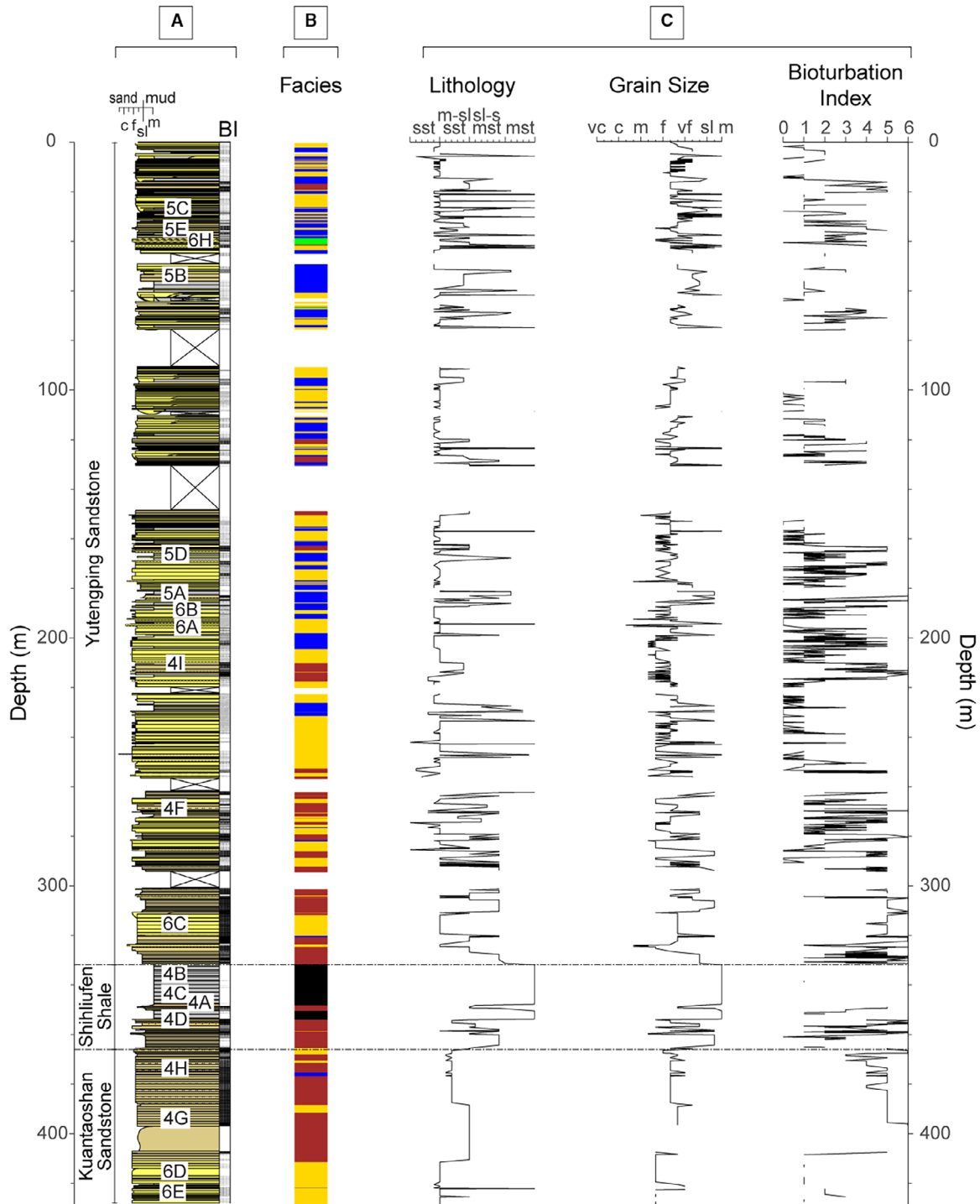#### Bioturbated sandy mudstone to muddy sandstone (facies 2)
*Description.* Facies 2 (Fig. 4) comprises bioturbated sandy mudstone to muddy sandstone. Physical sedimentary structures are typically not preserved owing to pervasive bioturbation. The exceptions to this are uncommon intercalations of sharp-based, planar parallel to cross-laminated and hummocky cross-stratified (HCS) sandstone beds. In Facies 2b, these sandstone interbeds are typically capped by massive to wavy parallel-laminated mudstone drapes. Bioturbation intensities are moderate to high (BI 3 to 5), except in the laminated sandstone interbeds (BI 0 to 2). Disarticulated bivalve, crab and gastropod fossils, as well as coal fragments occur throughout Facies 2 but are particularly common in Facies 2a. Additionally, shell hash and rip-up clasts, as well as abundant *Ditrupa* tubes are found in Facies 2a in the Kuantaoshan Sandstone. The trace fossils identified in Facies 2 are *Asterosoma*, *Chondrites*, *Ophiomorpha*, *Phycosiphon*, *Planolites*, *Rosselia*, *Schaubcylindrichnus coronus*, *Schaubcylindrichnus freyi*, *Skolithos*, *Teichichnus* and *Thalassinoides*. Some units also have *Diplocraterion* or *Scolicia*.

*Interpretation.* The highly bioturbated sandy mudstone and muddy sandstone of Facies 2 reflect deposition in upper offshore (F2a) to distal delta front (F2b) environments near but below fairweather wave base. Conditions with limited fluvial influence allowed for thorough bioturbation of the seafloor by a highly diverse palaeo-community of trace-making organisms, which led to the destruction of most primary sedimentary structures through sediment reworking (Bann *et al.*, 2004; Bann & Fielding, 2004). Where preserved, laminated sandstone beds probably reflect either sediment reworking by large waves or elevated sedimentation via fluvial discharge associated with tropical cyclones (Dashtgard *et al.*, 2020; Vaucher *et al.*, 2023a). The dark, carbonaceous mudstone drapes and the presence of coal fragments are rare in F2a but more commonly observed in F2b, suggesting that F2b records enhanced influence of fluvial discharge compared to F2a. Such mudstones are likely fluid mud layers deposited from hypopycnal plumes during river floods from heightened precipitation that commonly accompany storms (MacEachern *et al.*, 2005; Bhattacharya & MacEachern, 2009; MacEachern & Bann, 2020). The presence of laminated sandstone beds, agglomerations of *Ditrupa* tubes, disarticulated shell hash, coal fragments and rip-up clasts reflects storm influence.

#### Lenticular-bedded, wavy-bedded and flaser-bedded heterolithic bedsets (facies 3)
*Description.* Facies 3 comprises lenticular-bedded to wavy-bedded heterolithic bedsets of mudstone and silty sandstone (F3a) and wavy-bedded to flaser-bedded heterolithic bedsets of sandstone with mudstone (F3b; Fig. 5;

**Fig. 2.** Outcrop (A) and facies (B) logs of the Kueichulin Formation outcrop along the Da'an River with sedimentary data (C) in the depth domain. Dashed lines denote upper (332.3 m) and lower (366.3 m) boundaries of the Shihliufen Shale. White intervals in the facies log denote inaccessible, covered or collapsed outcrop sections. Acronyms: [lithology] mudstone (mst); silty to sandy mudstone (sl–s mst); muddy to silty sandstone (m–sl sst); sandstone (sst) | [grain size] mud (m); silt (sl); very fine-grained (vf); fine-grained (f), medium-grained (m); coarse-grained (c); very coarse-grained (vc) | [ichnology] bioturbation index (BI). Text on the outcrop log denotes positions of facies photos in Figs 4 to 6.
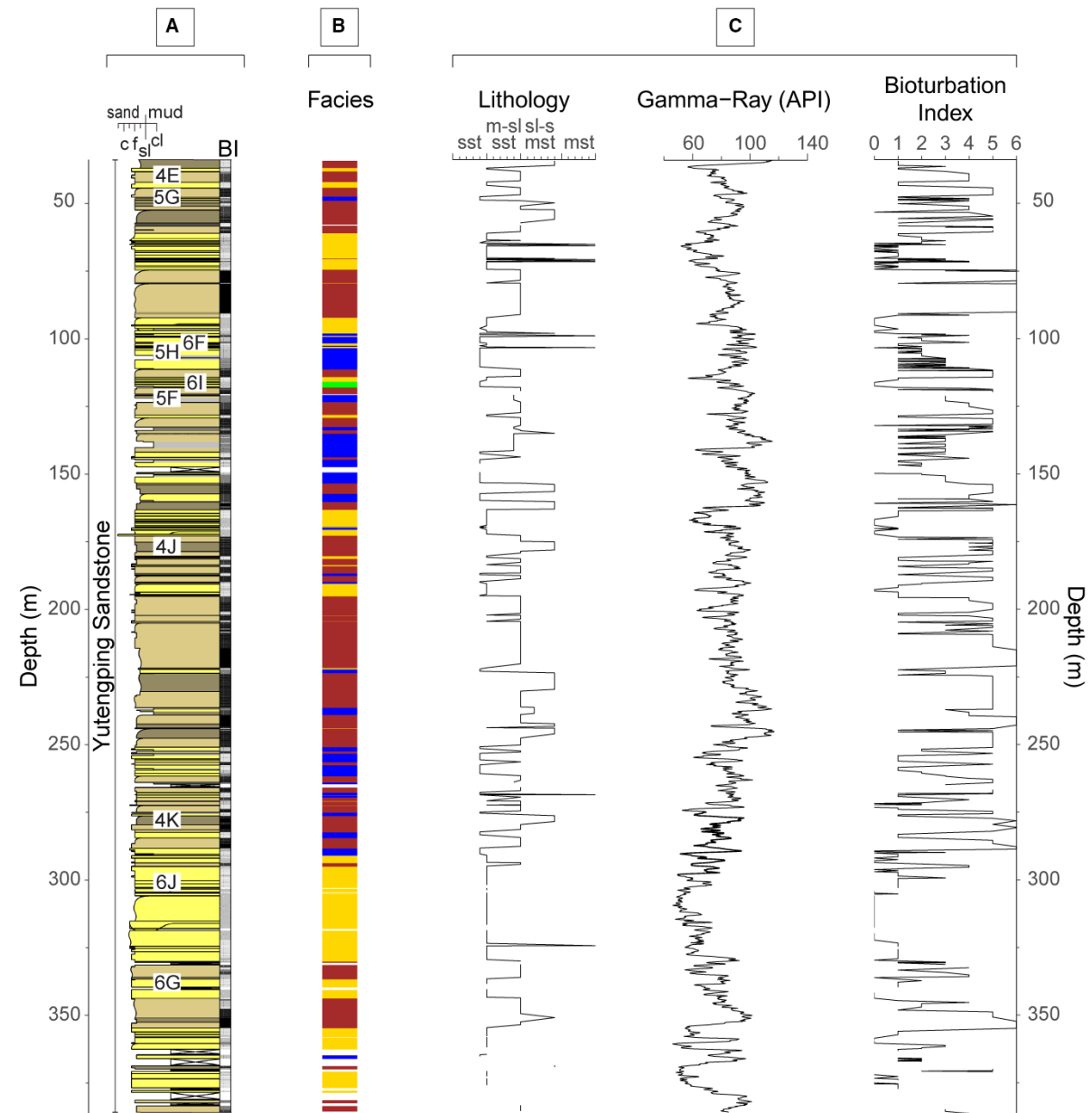
Table 1). Sharp-based, massive and planar to wavy parallel-laminated mudstone beds with rare inverse grading are interbedded with current-rippled to wavy parallel laminated (F3a) or massive to parallel-laminated and current-rippled (F3b) sandstone beds. Facies 3b sandstone layers also exhibit uncommon trough to low-angle planar tabular cross-stratification and HCS. Sandstone beds typically have erosive basal surfaces. Bioturbation occurs as largely top-down burrowing and is typically confined to mudstone-rich beds. BI ranges from 1 to 3 in the mudstone beds and BI ranges from 0 to 1 in the laminated sandstone beds. Rare mudstone rip-up clasts, disarticulated bivalve shell fragments and coal fragments are also found in the laminated sandstone beds. Trace fossils identified in the facies include rare *Arenicolites*, *Asterosoma*, *Chondrites*, *Ophiomorpha*, *Phycosiphon*, *Planolites*, *Rosselia*, rare *Schaubcylindrichnus* and *Thalassinoides*.

*Interpretation.* Facies 3 is interpreted to record delta-front deposition in a tidal strait with increased sediment supply from Taiwan and relative shallowing of the WFB. Fluvial influence increases from Facies 3a to 3b. The heterolithic mudstone and sandstone reflect fluctuating energy conditions with repeated waning of unidirectional to oscillatory flow (Vaucher *et al.*, 2023a). The erosive-based, massive to laminated sandstone beds represent deposition under high-energy, unidirectional flows with high sediment loads (Bann & Fielding, 2004; Dashtgard *et al.*, 2020). Decreasing energy conditions led to deposition of current-ripple laminated sandstone and mudstone drapes through suspension settling. Laminated and inversely graded mudstone beds reflect rapid deposition, possibly from hyperpycnal plumes (Bentley, 2003; Bhattacharya & MacEachern, 2009; Castelltort *et al.*, 2011; Bhattacharya *et al.*, 2020). The presence of rip-up clasts, disarticulated bivalve shell fragments and coal fragments is consistent with high-energy conditions. The paucity of bioturbation and

presence of diminutive trace fossils indicate stressed conditions, which may indicate intermittent high-energy conditions, rapid sedimentation rates and/or chemical stresses (e.g. salinity fluctuations associated with fluvial input; MacEachern & Bann, 2020, 2023). Facies 3 represents deposition in shallower water relative to the highly bioturbated sandy mudstone and muddy sandstone of Facies 2. Water depth estimates for Facies 3 range from 10 to 20 m (Nagel *et al.*, 2013; Dashtgard *et al.*, 2021).

### Massive (structureless) to stratified sandstone (facies 4)

*Description.* Two expressions of Facies 4 are found in the Yutengping Sandstone (Fig. 6; Table 1). The first is massive (structureless) or low-angle planar cross-stratified to trough cross-stratified sandstone or silty sandstone (F4a). Foresets show multiple dip directions but dominantly towards the north or south. The bases of the trough cross-bedded sandstone are sharp and commonly truncate underlying strata. Wave ripples are also common towards the tops of beds and are locally aggradational. The second expression of the Facies 4 deposit (F4b) comprises sharp-based, amalgamated, planar parallel to hummocky cross-stratified sandstone beds that typically grade upwards into current-rippled (locally aggradational) sandstone. In both F4a and F4b, sandstone beds are commonly capped by carbonaceous, apparently structureless to laminated, sharp-based mudstone. Plant debris, mudstone rip-up clasts, coal clasts and shell fragments are commonly found throughout the sandstone beds and are commonly concentrated towards their bases. In F4a, sandstone beds rich in disarticulated bivalve shell fragments and shell hash are common. Mudstone beds are locally entirely made of carbonaceous material. Bioturbation intensities range from BI 0 to 2 and primarily record top-down colonization of the bed. Trace fossils are dominated by *Ophiomorpha*, *Rosselia* and *Thalassinoides* with

**Fig. 3.** Core (A) and facies (B) logs of the cored interval through the Kueichulin Formation at TCDP-A with sedimentary data (C) in the depth domain. White intervals in the facies log denote inaccessible, covered or collapsed outcrop sections. Acronyms: [lithology] mudstone (mst); silty to sandy mudstone (sl–s mst); muddy to silty sandstone (m–sl sst); sandstone (sst) | [grain size] mud (m); silt (sl); very fine grained (vf); fine grained (f), medium grained (m); coarse grained (c); very coarse grained (vc) | [ichnology] bioturbation index (BI). Text on the outcrop log denotes positions of facies photos in Figs 4 to 6.

subordinate *Cylindrichnus*, fugichnia, and *Macaronichnus* isp. *Chondrites* and *Planolites* occur locally and are largely confined to the mudstone beds.

*Interpretation.* The sharp-based, massive cross-bedded sandstone of Facies 4a is interpreted as intervals of amalgamated dunes that formed under rapid deposition and unidirectional flow (Nagel *et al.*, 2013; Vaucher & Dashtgard, 2022). Aggradational wave ripples form during deceleration of bottom currents, high sedimentation and a transition to oscillatory flow (Myrow & Southard, 1996; Myrow *et al.*, 2002; Nagel *et al.*, 2013). Sharp-based, massive to laminated mudstone beds are interpreted as fluid mud deposited from the hypopycnal plumes discharged from fluvial sources (Bentley, 2003; MacEachern *et al.*, 2005; Bhattacharya *et al.*, 2020; MacEachern & Bann, 2020). Mudstone rip-up clasts and coal clasts in the sandstone beds are consistent with high-energy flow conditions and sediment input from nearby rivers during storm or post-storm flooding (Collins *et al.*, 2017; Lin & Bhattacharya, 2021; Vaucher *et al.*, 2023a). The paucity of bioturbation and low-diversity marine trace fossil suites indicate that animals were subjected to physico-chemical stresses such as intermittent high-energy conditions, rapid sedimentation rates and/or salinity fluctuations associated with fluvial influence (e.g. Bann *et al.*, 2004; MacEachern *et al.*, 2005, 2007). The defining features of Facies 4a indicate a shallow-marine environment with a proximal terrestrial sediment source under high-energy conditions with elevated sediment loads. Facies 4a shares similar features as tropical cyclone deposits described in the WFB by Dashtgard *et al.* (2020).

Facies 4 is interpreted as event beds that record deposition in the delta front during tropical cyclones. Specifically, deposition occurred under high-energy unidirectional-flow, oscillatory-flow and/or combined-flow conditions coupled with an elevated sediment supply in positions well above fairweather wave base. Facies 4a represents rapid sedimentation from flows with high suspended-sediment concentrations developed during tropical cyclones. F4b records deposition under lower sediment concentrations and is subjected to a range of processes that were active during and after tropical cyclones (e.g. Hayes, 1967; Dashtgard *et al.*, 2020). Aggradational wave and combined-flow ripples indicate high and continuous sediment supply. Aggrading wave ripples may preferentially form near the outer rainband of a tropical cyclone, where wind velocities are relatively low (Vaucher *et al.*, 2023a). Specifically, under low wind velocities and above fair-weather wave base, unidirectional currents at the seafloor are typically lower, which allows for oscillatory wave motion to dominate. Near the eyewall of tropical cyclones, wind velocities are high, and therefore, unidirectional currents dominate (Mitchell *et al.*, 2005; Teague *et al.*, 2007; Dashtgard *et al.*, 2020). The amalgamated laminated sandstone beds were likely deposited by successive storm events that scoured into underlying storm beds. The sharp-based, massive to laminated mudstone beds that cap underlying sandstone beds reflect both deposition from hyperpycnal flows and post-storm hypopycnal plumes, both of which are sourced from rivers on Taiwan (Dashtgard *et al.*, 2020). The low bioturbation intensities, presence of escape structures and presence of rip-up clasts and organic debris are consistent with high depositional energy and rapid sedimentation (Dashtgard *et al.*, 2020).

### Soft-sediment deformed beds (facies 5)

*Description.* Facies 5 represents soft-sediment deformation (SSD) in delta-front deposits (Fig. 6; Table 1). Soft-sediment deformation structures observed in the Kueichulin Formation include convolute bedding and ball-and-pillow structures. Primary sedimentary structures and evidence of bioturbation are rarely preserved in the SSD beds.
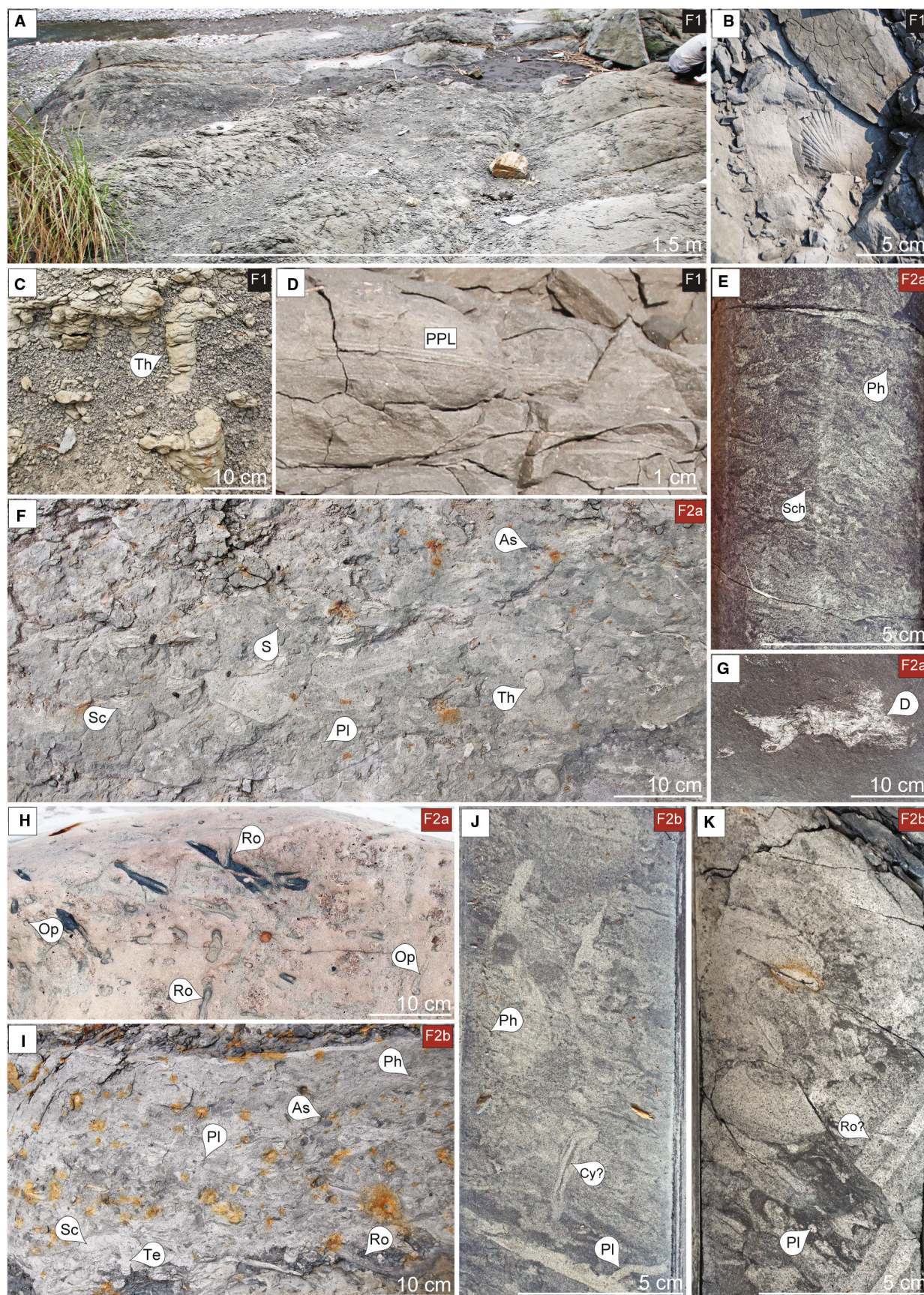
**Fig. 4.** Facies 1 and 2. (A–D) Pervasively bioturbated mudstone of F1 with mud-filled *Thalassinoides*. (E–H) Bioturbated muddy sandstone to sandy mudstone of Facies 2a showing intense bioturbation. *Ditrupa* tubes (D in photo G) are abundant in F2a of the Kuantaoshan Sandstone. Shell fragments (S) are found in F1 and F2. (I–K) Bioturbated muddy sandstone to sandy mudstone with mudstone interbeds (F2b). Trace fossils acronyms include: *Asterosoma* (As),*? Cylindrichnus* (Cy?), *Ophiomorpha* (Op), *Phycosiphon* (Ph), *Planolites* (Pl), *Rosselia* (Ro), *Schaubcylindrichnus* (Sch), *Scolicia* (Sc), *Teichichnus* (Te) and *Thalassionides* (Th). Acronym for planar parallel lamination is PPL. Locations of the photos are shown along the outcrop/core sections.

*Interpretation.* The SSD structures documented in the Kueichulin Formation indicate post-depositional liquefaction of unconsolidated sediment related to rapid sediment loading or disturbance of water-saturated sediment. Driving mechanisms of SSD include rapid deposition, groundwater movement, strong currents, storm activity, rapid changes in temperature and sediment-gravity mass movements (Mills, 1983; Owen *et al.*, 2011; Shanmugam, 2017 and references therein).

**Time-series analysis**

The Kuantaoshan Sandstone (~6300 to 5400 Ka) was deposited during a period of low obliquity and high precession amplitudes and relatively stable global mean sea-level, and comprises dominantly Facies 2 and 4 (Fig. 7). Lithology, grain size and BI through the Kuantaoshan Sandstone show minimal variability. The Shihliufen Shale (~5400 to 4920 Ka) along the Da'an River comprises mostly Facies 1 and 2 (mudstone with high BI values), which coincides with maximum obliquity amplitudes but shows no apparent relationship with changes in precession or sea-level amplitudes (Fig. 7B, E, and F). Through the Yutengping Sandstone at the Da'an River outcrop (~4920 to 4130 Ka), strata dominated by Facies 2 transition upwards into Facies 3 with decreasing obliquity amplitudes at ~4750 Ka (Fig. 7B and E). Variability in facies and facies characteristics is high through the Yutengping Sandstone and decreases after ~4300 Ka, coinciding with minimum obliquity amplitudes. Thick successions of Facies 4 in the Yutengping Sandstone tend to coincide with periods of increasing precession amplitudes and highly variable insolation based on comparison to the p-0.5 t curve (e.g. ~4800 to 4750 Ka, and ~4265 to 4225 Ka; Fig. 7D, E, and F). Changes in background facies (i.e. F1 to 3) at the Da'an river outcrop, however, do not appear to be related to long-term (i.e. >100-kyr) changes in global mean

sea-level (Fig. 7F). Intervals of Facies 5 are rare and show no relationship to orbital cyclicity or insolation.

At TCDP-A, strata of the Yutengping Sandstone show that deposition of thoroughly bioturbated, fine-grained sediment of Facies 1 and 2 is more common during periods of low obliquity amplitudes and corresponds with high global mean sea-level (e.g. ~4620 to 3950 and ~3360 to 3154 Ka; Fig. 8B, C, E, and F). Deposition of Facies 3 is more prevalent during high obliquity amplitude and also corresponds to high sea-level (e.g. ~3840 to 3410 Ka; Fig. 8B, E, and F). Similar to the Da'an River outcrop, expressions of Facies 4 and probable sandstone-dominated intervals identified on GR data tend to occur during periods of high insolation and precession maxima (e.g. ~4920 to 4850, ~4750 to 4640 and ~3320 to 3260 Ka; Fig. 8D and E), and were best preserved during intervals when sea-level was low (e.g. ~5000 to 4650 and 3320 to 3250 Ka). In addition, variability in facies, lithology, GR and BI values is highest with increasing obliquity and sea-level amplitudes (e.g. ~5000 to 4370 and 3950 to 3410 Ka). As at the Da'an River location, the influence of long-term (>100-kyr) sea-level change is not reflected clearly in shifts in the background facies. Intervals of Facies 5 are rare and appear to be independent of orbital cyclicity and insolation.

The filtered, astronomically tuned datasets for the Kueichulin Formation are used to assess the amplitude (strength) of orbital components preserved in the sedimentary record (Figs S3 and S4). In the Da'an River outcrop, precession and obliquity amplitudes are low between ~5350 and 5000 Ka in all datasets (Fig. S3). At TCDP-A, the facies record shows that precession and eccentricity amplitudes are lowest from ~4600 to 4000 Ka with the deposition of shallow-marine deltaic facies with limited tide influence, while obliquity amplitudes appear to be strong throughout the rest of the succession except at a minimum near ~4200 Ka (Fig. S4). The
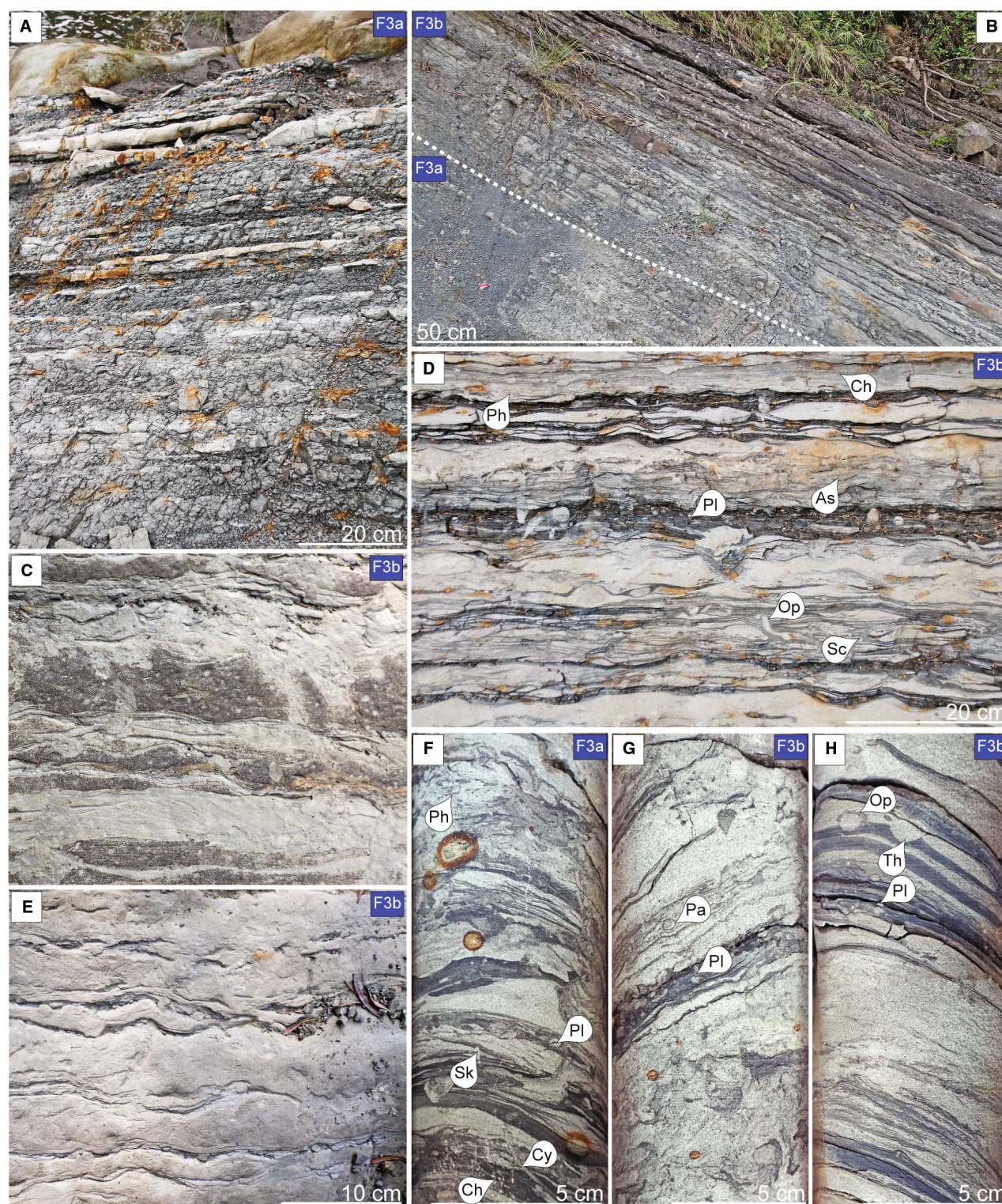
**Fig. 5.** Facies 3. (A) Lenticular-bedded to wavy-bedded mudstone and (silty) sandstone of F3a. (B) F3a transitioning upwards into F3b. (C–E) Examples of wavy-bedded to flaser-bedded heterolithic bedsets of F3b. (F–H) Photographs of F3a and F3b expressed in core. Trace fossils include *Asterosoma* (As), *Chondrites* (Ch), *Cylindrichnus* (Cy), *Ophiomorpha* (Op), *Phycosiphon* (Ph), *Planolites* (Pl), *Scolicia* (Sc), *Skolithos* (Sk) and *Thalassionides* (Th). Locations of the photos are shown along the outcrop/core sections.
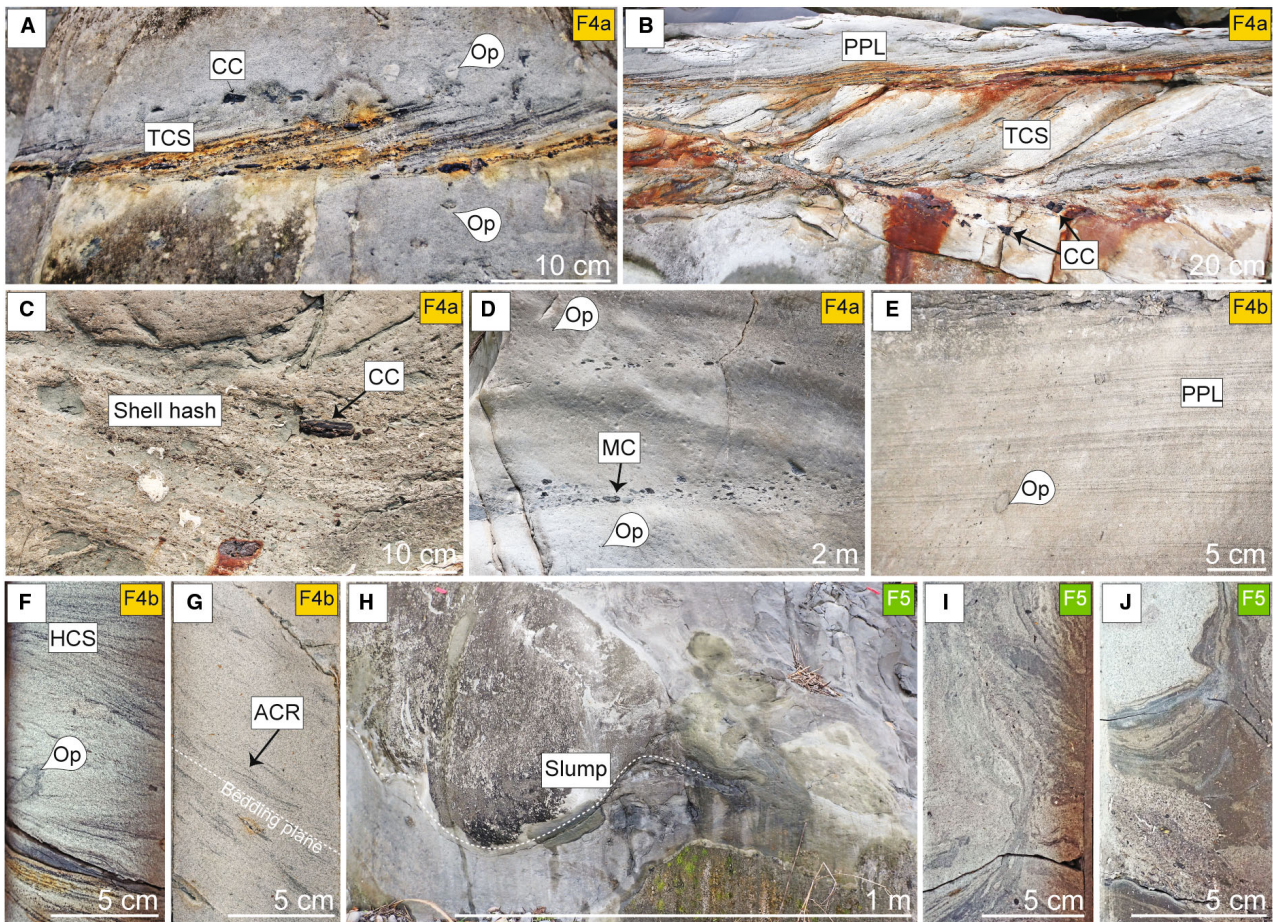
**Fig. 6.** Facies 4 and 5. (A–C) Trough cross-stratified and (D) planar parallel laminated sandstone deposited during and immediately following tropical cyclones. Abundant mudstone and coal rip-up clasts as well as shell hash are present throughout. (E) Thick successions of massive (structureless) sandstone are delineated by large rip-up clasts. (F) Hummocky cross-stratified sandstone. (G) Aggradational current ripples. (H–J) Soft-sediment deformation structures shown in outcrop and core examples. Trace fossils shown in photos are *Ophiomorpha* (Op). Acronyms for sedimentary structures and accessories used include aggradational current ripple (ACR), coal clast (CC), hummocky cross-stratification (HCS), mud (rip-up) clast (MC), planar parallel lamination (PPL), trough cross-stratification (TCS). Locations of the photos are shown along the outcrop/core sections.

GR, lithology and BI record high orbital amplitudes except between ~4300 and 4000 Ka (Fig. S4B–D).

## DISCUSSION: LATE-MIOCENE TO PLIOCENE EVOLUTION OF THE TAIWAN WESTERN FORELAND BASIN DEPOSITIONAL ENVIRONMENT

### Orogenesis and basin subsidence

The Kueichulin Formation (i.e. palaeo-Taiwan Strait) records sedimentation under depositional settings that vary from a wave-dominated open shelf to tide-dominated shallow-marine deltas with strong storm influence and increasing terrestrial sediment input. The shifting of depositional settings was strongly controlled by both the rate of basin subsidence and the uplift and erosion of Taiwan since its formation. At the onset of collision between the Eurasian Plate and the Philippine Sea Plate (~6270 Ka; Lin & Watts, 2002; Lin *et al.*, 2003; Nagel *et al.*, 2013; Hsieh *et al.*, 2023a), deposition of the Kuantaoshan Sandstone occurred in mainly an open marine, upper offshore (F2a) environment repeatedly impacted by tropical cyclones (F4). The development of offshore (F1) to distal delta front (F2b) environments with limited fluvial

**Fig. 7.** Outcrop and facies logs of the Kueichulin Formation outcrop along the Da'an River in the depth domain (A). Age boundaries from Hsieh *et al.* (2023a) were used to constrain the sedimentary facies (B) and data (C) in the time domain. The p-0.5 t curve (D) is the mix-standardized precession minus 0.5 times of standardized obliquity, w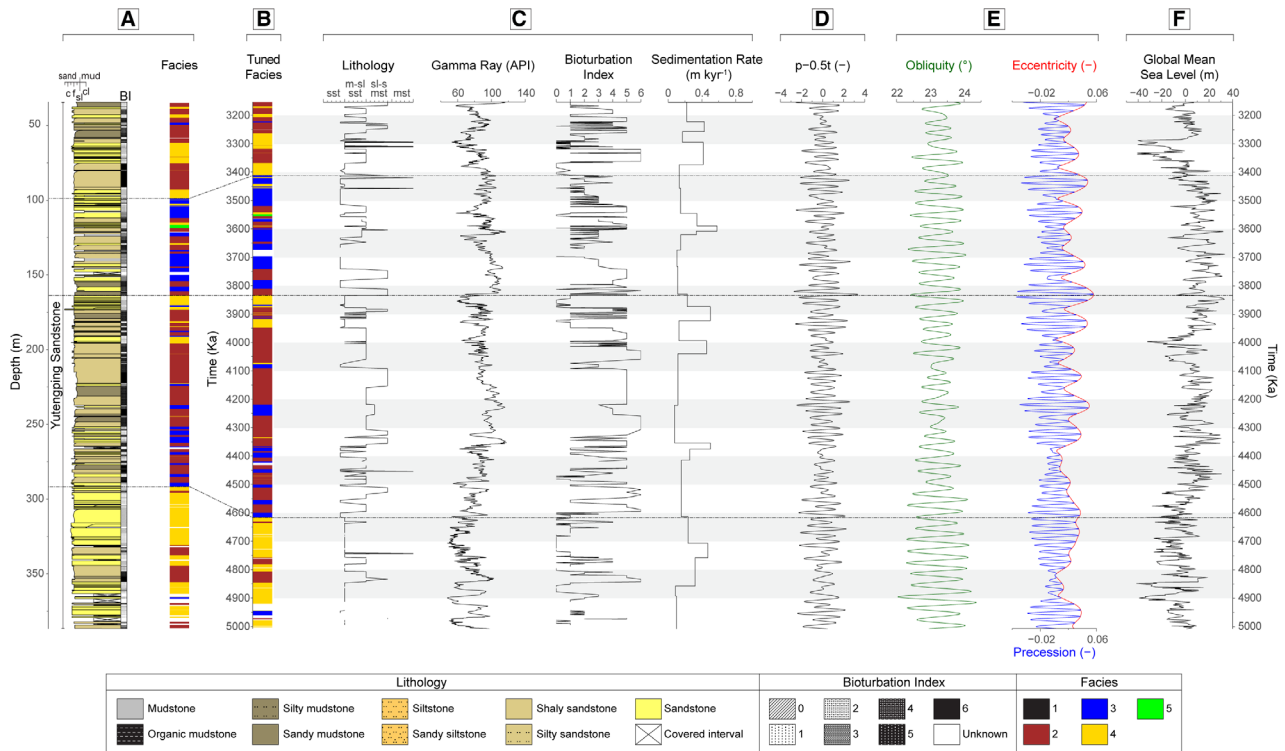hich represents ~65° N insolation (Laskar *et al.*, 2004). Astronomical solutions for the Earth's obliquity, eccentricity and precession for the studied time interval are from Laskar *et al.* (2004) (E). Global mean sea-level is from Miller *et al.* (2020) (F). The facies and sedimentary data in the time domain are compared to the p-0.5 t curve, orbital solutions and global mean sea-level to evaluate their control on shifting depositional environments. Dash-dot lines indicate boundaries between major shifts in depositional settings interpreted from facies. White intervals in the facies log denote inaccessible, covered or collapsed outcrop sections. Acronyms: [lithology] mudstone (mst); silty to sandy mudstone (sl–s mst); muddy to silty sandstone (m–sl sst); sandstone (sst) | [grain size] mud (m); silt (sl); very fine grained (vf); fine grained (f), medium grained (m); coarse grained (c); very coarse grained (vc) | [ichnology] bioturbation index (BI).

influence, as recorded in the Shihliufen Shale, reflects the non-linear deepening of the WFB (Lin *et al.*, 2003). Relative sedimentation from the newly emergent Taiwan into the basin fluctuated in response to the rate of basin acceleration and accommodation space. The deepening of the basin also resulted in deposition below fairweather wave base and near to, but generally above, storm wave base.

Taiwan began to rapidly emerge from the Pacific Ocean and erode starting ~4920 Ka (Hsieh *et al.*, 2023a). Emergence of Taiwan resulted in an increase in accommodation space,

as the WFB deepened, and progradation into and filling of the basin is recorded in the Yutengping Sandstone (Lin *et al.*, 2003). The emergence of Taiwan also caused the shallowing and narrowing of the palaeo-Taiwan Strait. Tidal influence was limited during the deposition of the lower part of the Yutengping Sandstone, while storm influence was high. This interpretation is supported by the dominance of distal delta front facies (F2b), abundant tropical cyclone beds (F4), and a paucity of sedimentary structures that indicate tidal influence. Tidal flow strengthened in the palaeo-Taiwan Strait

**Fig. 8.** Core and facies logs of the cored interval through the Kueichulin Formation at TCDP-A in the depth domain (A). Age boundaries from Hsieh *et al.* (2023a) were used to constrain the sedimentary facies (B) and data (C) in the time domain. The p-0.5 t curve (D) is the mix-standardized precession minus 0.5 times of standardized obliquity, which represents ~65° N insolation (Laskar *et al.*, 2004). Astronomical solutions for the Earth's obliquity, eccentricity and precession for the studied time interval are from Laskar *et al.* (2004) (E). Global mean sea-level is from Miller *et al.* (2020) (F). The facies and sedimentary data in the time domain are compared to the p-0.5 t curve, orbital solutions and global mean sea-level to evaluate their control on shifting depositional environments. Dash-dot lines indicate boundaries between major shifts in depositional settings interpreted from facies. White intervals in the facies log denote inaccessible, covered or collapsed outcrop sections. Acronyms: [lithology] mudstone (mst); silty to sandy mudstone (sl–s mst); muddy to silty sandstone (m–sl sst); sandstone (sst) | [grain size] mud (m); silt (sl); very fine grained (vf); fine grained (f), medium grained (m); coarse grained (c); very coarse grained (vc) | [ichnology] bioturbation index (BI).

with the continued shallowing and narrowing of the strait as Taiwan continued to uplift. This is recorded in the upper part of the Yutengping Sandstone through an increase in tidally dominated delta-front deposits (F3).

At the Da'an River outcrop, the abrupt shift from strata dominated by Facies 1 and 2 of the Shihliufen Shale to Facies 3-dominated strata in the Yutengping Sandstone is interpreted as the transition from deposition near to but above storm base (100 m water depth) to deposition in water depths possibly above fairweather wave base (15 m water depth; Nagel *et al.*, 2013). Firstly, the trend of decreasing water depth upwards (with decreasing age) reflects an overall relative shallowing of the depositional

environment as a function of depositional regression and progradation of facies, but long-term sea-level remained relatively stable over this time period. The long-term (>100 kyr) increase in sea-level after ~4600 Ka is also not reflected in the sedimentary record (Fig. 7), probably because the rate of sediment delivery began to outpace the creation of accommodation space. This can result in reduced expression of sea-level change as excess sediment supply dampens the stratigraphic response to sea-level changes, leading to subdued or entirely absent markers of transgression or regression. Likewise, at the TCDP-A location, the shift from strata dominated by Facies 2 to those of Facies 3, interpreted as a shift from wave-dominated to
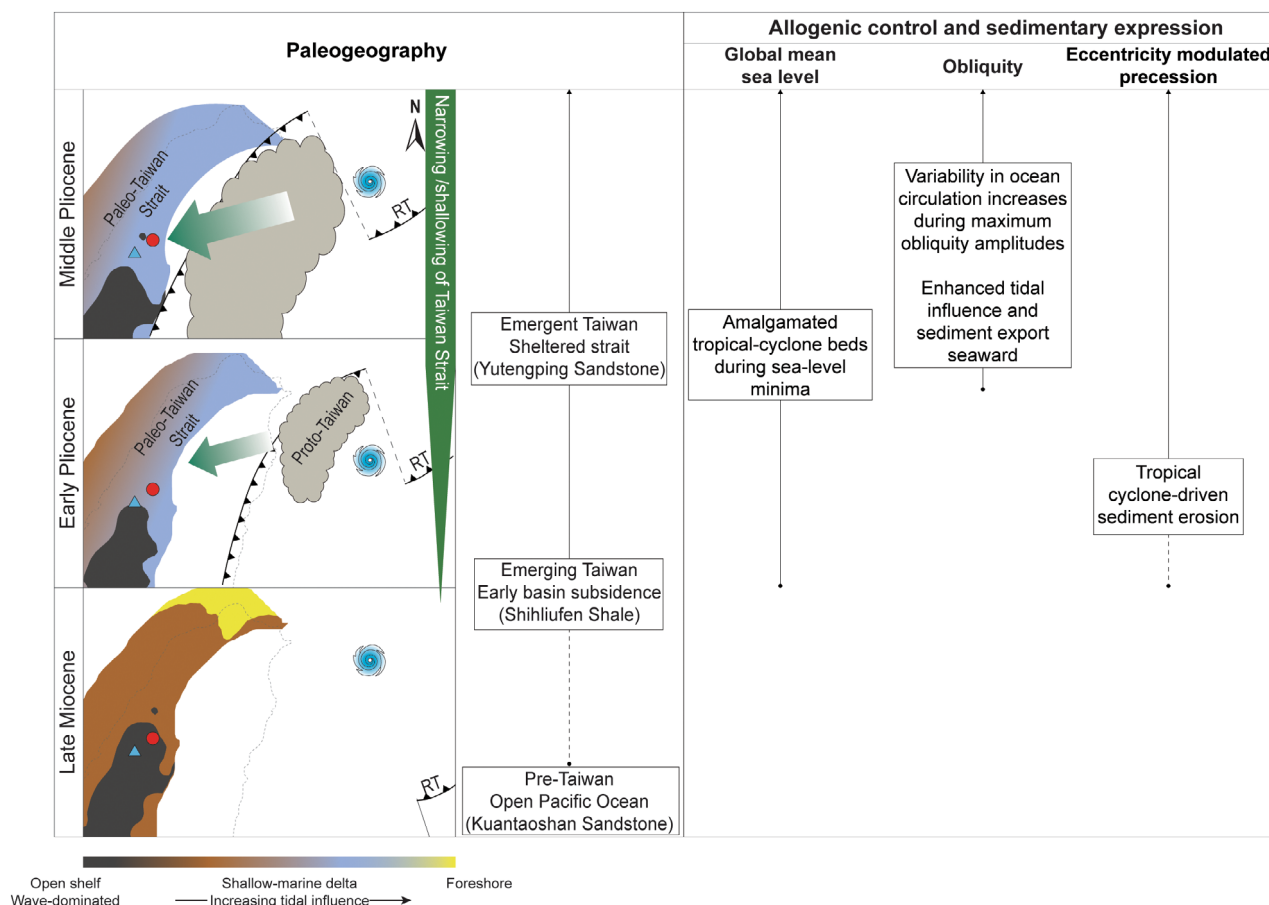
**Fig. 9.** Summary of different allogenic controls on sedimentation in the Western Foreland Basin over time. The red circle and the blue triangle indicate the present-day locations of the Da'an River outcrop and the TCDP-A core, respectively. The size of the green arrows indicates relative proportions of sediment flux into the Western Foreland Basin eroded by tropical cyclones from the Taiwan Orogen. The abbreviation RT denotes the Ryukyu Trench. Spatial distribution of sedimentary environments modified from Nagel *et al.* (2013), and the timing of tectonic events related to the orogenesis of Taiwan are from Lin *et al.* (2003) and Hsieh *et al.* (2023b).

tide-dominated shallow-marine deltaic environments, occurred under similar long-term global mean sea-levels.

The discrepancies in facies expressions and thicknesses between the Da'an River outcrop and the TCDP-A core are interpreted to reflect their positions relative to Taiwan and the Taiwan Strait (Fig. 9). The Da'an River outcrop is located farther inland of the modern Taiwan Orogen than TCDP-A (Fig. 1). By extension, it is probable that during the deposition of the Kueichulin Formation in the late Miocene–Pliocene, the Da'an River location was more proximal to Taiwan and the TCDP-A location was situated farther seaward in the palaeo-Taiwan Strait. Therefore, the sedimentary environment at the Da'an River responded earlier to tectonic changes related to

the uplift of Taiwan than did the locality at TCDP-A. At the Da'an River location, sedimentation occurred closer to the Taiwan Orogen where tidal currents were stronger and terrestrial organic matter flux was higher (probably similar to today). This resulted in the transition from a wave-influenced to a tidally influenced depositional environment with increasing fluvial influence occurring much earlier (~4750 Ka) than at TCDP-A (~4620 Ka; Fig. 8).

## Influence of eccentricity-modulated precession on hydroclimate

Sedimentation into the WFB is also strongly tied to low-latitude hydroclimate (Dashtgard *et al.*, 2021; Vaucher *et al.*, 2023a; Hsieh *et al.*, 2023b).

Firstly, conditions for tropical-cyclone genesis in the north-western Pacific were favourable in the Pliocene (Yan *et al.*, 2019), as weaker Walker Circulation drove El-Niño-like conditions (Kaboth-Bahr & Mudelsee, 2022), and sea surface temperatures were higher than the present day, with an average of 28.5°C (Li *et al.*, 2011). Secondly, marine and continental records suggest that the East Asian Summer Monsoon intensified during the late Miocene to Pliocene (e.g. Filippelli, 1997; Wan *et al.*, 2006, 2010; Zhang *et al.*, 2009; Ao *et al.*, 2011, 2016; Gai *et al.*, 2020), and this has been attributed to the growth of the Antarctic ice sheet (Ao *et al.*, 2016), phased uplift events in the Tibetan Plateau (Prell & Kutzbach, 1992; An *et al.*, 2001; Sun *et al.*, 2010), the closure of the Central America Seaway (Gai *et al.*, 2020), the formation of the Western Pacific Warm Pool (Chaisson & Ravelo, 2000; Li *et al.*, 2004; Jian *et al.*, 2006) and the northward migration of the Intertropical Convergence Zone (Liu *et al.*, 2019). With enhanced conditions for tropical-cyclone and monsoon precipitation, rainfall extremes will likely trigger enhanced fluvial run-off and sediment discharge (Lee *et al.*, 2015). As global tropical-cyclone activity is the most enhanced in the western north Pacific ocean, and most cyclones form within or near the monsoon trough (Chen *et al.*, 2010), rainfall extremes may be amplified if a tropical cyclone interacts with summer monsoon precipitation (Wu *et al.*, 2011; Vaucher *et al.*, 2021). Tropical cyclone activity is preserved as thick successions of massive (structureless) to stratified sandstone beds with high proportions of terrestrial organic matter (i.e. F4). Tropical cyclone beds are preserved throughout the Kuantaoshan Sandstone and the Yutengping Sandstone, reflecting deposition above fair-weather wave base and above storm wave base. In contrast, in the Shihliufen Shale, storm-generated sedimentary structures are uncommon due to deeper water depths related to basin subsidence and may represent distal expressions of tropical cyclone deposits.

The presence of tropical cyclone beds typically corresponds to periods of maximum precession amplitudes and eccentricity (e.g. ~4265 to 4225 Ka at Da'an River and ~4750 to 4640 Ka at TCDP-A; Figs 7 and 8), except during periods of low global mean sea-level. Extreme sea-level minima led to an increased export of coarse-grained fractions and shoreline progradation, resulting in enhanced preservation of amalgamated tropical cyclone beds even during periods

of moderate precession amplitudes. This is clearest at TCDP-A, where tropical cyclone beds are less commonly expressed due to its more distal position from the Taiwan Orogen, except during periods of global mean sea-level minima (e.g. ~5000 to 4650 and 3320 to 3250 Ka; Fig. 8).

Precession amplitudes in the filtered datasets are lower in the Kuantaoshan Sandstone than in the Yutengping Sandstone (Fig. S3). This is because prior to the onset of Taiwan orogenesis (~5400 Ka), sediment in the WFB was susceptible to reworking by waves from the Pacific Ocean, resulting in increased amalgamation of tropical cyclone beds and obscuring precession signals preserved in the strata (Fig. 7). The onset of rapid erosion of the Taiwan Orogen by tropical cyclones began as soon as it emerged from the Pacific Ocean (~4920 Ka), increasing sediment influx into the WFB. The emergence of Taiwan also created a semi-sheltered strait which shielded the basin from erosive waves of the Pacific Ocean (Hsieh *et al.*, 2023a). Consequently, evidence of precession-driven tropical cyclones is more clearly expressed through the Yutengping Sandstone, where variability is substantially higher (Fig. 7), and precession amplitudes are most clearly expressed (Fig. S3).

Precession amplitudes recorded in the Yutengping Sandstone along the Da'an River outcrop are distinctively clearer than those expressed in the TCDP-A cored succession (Figs S3 and S4), which supports the interpretation that sedimentation at both locations was influenced by storm events, but that the effect of tropical cyclone-related sediment flux was stronger at the Da'an River location due to its proximity to the orogen. Near the orogen, sediment deposition would have been more dominantly controlled by variations in sediment supply from Taiwan and sediment dispersal by precession-driven hydroclimate as similarly described higher in the stratigraphy in the Pliocene Chinshui Shale and the Pleistocene Cholan Formation (Vaucher *et al.*, 2021, 2023b). Cyclic components preserved in the Kueichulin Formation mainly fall within the Milankovitch Bands (Hsieh *et al.*, 2023a). Additionally, the record is also naturally influenced by other factors, especially higher frequency climate system fluctuations on time scales shorter than 20 kyr cycles. For the high-resolution gamma-ray data at TCDP-A, there is evidence of local cyclicity on shorter time scales (i.e. <20 kyr). Also, there are cyclicities that are longer than Milankovitch cycles, and quasi-cyclic components between the ~400 and ~100 kyr bands, and these are possibly related to a combination of local

tectonics and sedimentary variability between these period bands.

## Obliquity-induced variability in atmospheric and ocean circulation

In addition to active orogenesis and tropical cyclones, the strata of the WFB also record variability driven by obliquity amplitude. At mid to low latitudes, insolation is largely controlled by precession with limited influence from obliquity (Prell & Kutzbach, 1987; Clement *et al.*, 2004; Berger *et al.*, 2006; Tachikawa *et al.*, 2011; Gai *et al.*, 2020). However, palaeoclimate records from mid-latitude to low-latitude regions often reveal an obliquity signal (e.g. Lourens *et al.*, 1996; Bosmans *et al.*, 2015; Liu *et al.*, 2015; Zhang *et al.*, 2022; Hsieh *et al.*, 2023a), which has been attributed to high-latitude mechanisms even during the warmer Miocene and Pliocene when changes in ice volumes should be less pronounced (Demenocal & Rind, 1993; Tiedemann *et al.*, 1994).

In mid-latitude to low-latitude regions, obliquity-driven changes in depositional environments may be related to increased seasonal variability in insolation during periods of high obliquity amplitude. Intensified seasonal variability in insolation can drive extreme shifts in atmospheric and ocean circulation (Fedorov *et al.*, 2010; Coumou & Rahmstorf, 2012; Yan *et al.*, 2016; Kossin *et al.*, 2020), leading to increased fluctuations in sediment supply and dispersal (e.g. Dadson *et al.*, 2003; Hilton *et al.*, 2010; Kao *et al.*, 2014; Lin *et al.*, 2020), and by extension, shifts in depositional environments. Sedimentation in the South China Sea in the present day is sensitive to changes in atmospheric circulation, terrigenous input (e.g. Liu *et al.*, 2015) and ocean circulation in the Pacific Ocean (e.g. Qu, 2000; Qu *et al.*, 2006; Tian *et al.*, 2006).

At the Da'an River location, transitions from offshore to delta front environments as well as increasing tidal influence are related to Taiwan orogenesis. The transition from Facies 1 through 3 records progradation of the system and filling of the basin, so that relative water depths become progressively shallower. The proximity of the Da'an River location to the Taiwan Orogen also resulted in the sedimentary facies of the Yutengping Sandstone recording clear tidal influence near the onset of Taiwan's emergence from the Pacific Ocean, regardless of changes in obliquity or precession. In contrast, at the more distal TCDP-A location, the transition between a wave-dominated open shelf to a tide-dominated shallow-marine delta is more closely related to changes in obliquity amplitudes. In the modern-day Taiwan Strait, tidal currents fluctuate with monsoon wind intensities as well as surface currents operating in the strait (Chuang, 1985, 1986; Wang *et al.*, 2003, 2021; Lin *et al.*, 2005). During periods of high obliquity amplitudes, enhanced variability in atmospheric and ocean circulation may have served to amplify tidal currents in the palaeo-Taiwan Strait, resulting in the formation of tide-dominated environments farther into the strait. While the influence of obliquity on low-latitude circulation is evident in the sedimentary record of the Kueichulin Formation, the effects of obliquity-driven sea-level change are only expressed as amalgamated tropical cyclone beds during global mean sea-level minima. However, while the global sea-level reconstruction shows periods of high-amplitude sea-level change (e.g. ~40 m) through the studied time interval, these large-scale fluctuations typically occur over relatively short intervals of time (i.e. <20 kyr). Any influence on the facies by such short-lived sea-level fluctuations may not be always and/or systematically preserved due to an underestimation in water depths. Water depths estimated previously for the deposition of the Yutengping Sandstone are less than ~35 m (Nagel *et al.*, 2013; Dashtgard *et al.*, 2020, 2021), but true water depth may have been deeper. This is because global mean sea-level estimates show obliquity-scale fluctuations of up to ~40 m, which should result in quasi-periodic subaerial exposure of shallow marine depositional environments. However, no evidence of subaerial exposure is identified in the Yutengping Sandstone; therefore, it is possible that water depths were significantly deeper (i.e. >70 m). The facies characteristics of the WFB strata must then be attributed to more energetic currents in deeper water, which would be expected in the palaeo-Taiwan Strait. Tidal and ocean currents through the palaeo-Taiwan Strait would have been amplified by increased tropical cyclones (Zhang *et al.*, 2020), especially as the strait narrowed and shallowed with continued uplift of Taiwan (Yin *et al.*, 2021, 2023; Hsieh *et al.*, 2024).

## CONCLUSIONS

Changes in depositional environments can be controlled by multiple autogenic and allogenic drivers, and resolving the relative influence of

each is challenging. In this study of the Kueichulin Formation of the Taiwan Western Foreland Basin (i.e. palaeo-Taiwan Strait), we focus on identifying and resolving the competing influence of climate, tectonics and sea-level fluctuations on the sedimentary system at time scales exceeding 20 kyrs. Strata of the Kueichulin Formation preserve evidence of shifting depositional settings from wave-dominated open shelf to tide-dominated shallow-marine delta with strong storm influence and increasing terrestrial sediment input. Changes in the sedimentary environments during the late Miocene and Pliocene were strongly controlled by allogenic drivers, including the orogenesis of Taiwan and the formation of the foreland basin. As well, sediment supply is tied to precipitation through tropical cyclones, which are affected by eccentricity-modulated precession. Obliquity-driven changes in atmospheric and ocean circulation and their subsequent effect on sediment dispersal are also evident in the stratal record.

Sedimentation to the palaeo-Taiwan Strait was strongly linked to the uplift and emergence of Taiwan. Prior to the emergence of Taiwan from the Pacific Ocean, the sedimentary archive records largely wave-dominated open shelf environments affected by tropical cyclone events. The rapid deepening of the Western Foreland Basin (~5400 Ka) and relatively low sedimentation rates contributed to the formation of lower offshore to distal delta front environments with limited storm influence. As Taiwan emerged from the Pacific Ocean and began to rapidly erode since ~4920 Ka, increased sedimentation into the Western Foreland Basin and shallowing/narrowing of the palaeo-Taiwan Strait resulted in the strengthening of tidal flow and increased terrestrial input, which is recorded in the strata of the Yutengping Sandstone.

Additionally, time-series analysis suggests that evidence of astronomical forcing on sedimentation is preserved in strata of the Kueichulin Formation. Deposition in the Western Foreland Basin was strongly tied to tropical cyclone precipitation driven by eccentricity-modulated precession. Intense tropical cyclone activity is preserved as the formation of thick successions of massive (structureless) to stratified sandstone beds that are found throughout the Kueichulin Formation. The abundance of sandstone beds increases as the Taiwan Orogen emerged from the Pacific, suggesting that the orogen became susceptible to rapid erosion by tropical cyclones

at the onset of its emergence. While the depositional environments of the Western Foreland Basin do not appear to be sensitive to long-term (>100-kyr) changes in global mean sea-level, tropical cyclone beds in the Kueichulin Formation are best preserved at extreme lows in global mean sea-level. Sea-level minima led to an increased export of coarse-grained fractions and shoreline progradation and led to the formation of amalgamated tropical cyclone beds even during periods of moderate precession amplitudes. This suggests that obliquity-driven glacial cycles at high latitudes and corresponding sea-level change have limited influence on low-latitude sedimentary environments; however, true water depths may have been previously underestimated, resulting in the lack of apparent influence of obliquity-driven sea-level fluctuations on the Western Foreland Basin.

The strata of the Western Foreland Basin also record the influence of obliquity on low-latitude atmospheric and ocean circulation. Fluctuating seasonal insolation related to high obliquity amplitudes manifests in mid-latitude to low-latitude environments as unstable atmospheric and ocean circulation, which may have served to amplify tidal currents in the palaeo-Taiwan Strait, resulting in the formation of tide-dominated environments farther into the strait.

This study demonstrates that shallow-marine sedimentary records can provide an important archive for identifying and resolving competing external controls on sedimentary systems. The ability to disentangle the relative influence of different allogenic forcings on shifting depositional environments serves to enhance our understanding of how the Earth's surface responded to past climate changes, tectonic activity and sea-level fluctuations.

## ACKNOWLEDGEMENTS

## CONFLICT OF INTEREST

The authors declare no conflict of interest.

## DATA AVAILABILITY STATEMENT

The data that support the findings of this study are available from the corresponding author upon reasonable request.

## REFERENCES

An, Z., Kutzbach, J.E., Prell, W.L. and Porter, S.C. (2001) Evolution of Asian monsoons and phased uplift of the Himalaya-Tibetan Plateau since late Miocene times. *Nature*, **411**, 62–66.

Ao, H., Dekkers, M.J., Qin, L. and Xiao, G. (2011) An updated astronomical timescale for the Plio-Pleistocene deposits from South China Sea and new insights into Asian monsoon evolution. *Qua. Sci. Rev.*, **30**, 1560–1575.

Ao, H., Roberts, A.P., Dekkers, M.J., Liu, X., Rohling, E.J., Shi, Z., An, Z. and Zhao, X. (2016) Late Miocene–Pliocene Asian monsoon intensification linked to Antarctic ice-sheet growth. *Earth Planet. Sci. Lett.*, **444**, 75–87.

Armitage, J.J., Dunkley Jones, T., Duller, R.A., Whittaker, A.C. and Allen, P.A. (2013) Temporal buffering of climate-driven sediment flux cycles by transient catchment response. *Earth Planet. Sci. Lett.*, **369**, 200–210.

Bann, K.L. and Fielding, C.R. (2004) An integrated ichnological and sedimentological comparison of non-deltaic shoreface and subaqueous delta deposits in Permian reservoir units of Australia. In: *The Application of Ichnology to Palaeoenvironmental and Stratigraphic Analysis Special Publications 228* (Ed McIlroy, D.), pp. 273–310. Geological Society of London, London, UK.

Bann, K.L., Fielding, C.R., MacEachern, J.A. and Tye, S.C. (2004) Differentiation of estuarine and offshore marine deposits using integrated ichnology and sedimentology: Permian Pebbley Beach Formation, Sydney Basin, Australia. In: *The Application of Ichnology to Palaeoenvironmental and Stratigraphic Analysis Special Publications 228* (Ed McIlroy, D.), pp. 179–211. Geological Society of London, London, UK.

Bentley, S.J., Sr. (2003) Wave-current dispersal of fine-grained fluvial sediments across continental shelves: the significance of hyperpycnal plumes. In: *Siltstones, Mudstones and Shales: Depositional Processes and Characteristics* (Eds Scott, E.D., Bouma, A.H. and Bryant, W.R.), Vol. **1**, pp. 35–48. SEPM Society for Sedimentary Geology, Oklahoma, USA.

Berger, A., Loutre, M.F. and Melice, J.L. (2006) Equatorial insolation: from precession harmonics to eccentricity frequencies. *Clim. Past*, **2**, 131–136.

Bhattacharya, J.P. and MacEachern, J.A. (2009) Hyperpycnal rivers and prodeltaic shelves in the Cretaceous Seaway of North America. *J. Sediment. Res.*, **79**, 184–209.

Bhattacharya, J.P., Howell, C.D., MacEachern, J.A. and Walsh, J.P. (2020) Bioturbation, sedimentation rates, and preservation of flood events in deltas. *Palaeogeogr. Palaeoclimatol. Palaeoecol.*, **560**, 110049.

Bosmans, J.H.C., Hilgen, F.J., Tuenter, E. and Lourens, L.J. (2015) Obliquity forcing of low-latitude climate. *Clim. Past*, **11**, 1335–1346.

Burgess, P.M. and Prince, G.D. (2015) Non-unique stratal geometries: implications for sequence stratigraphic interpretations. *Basin Res.*, **27**, 351–365.

Castelltort, S., Nagel, S., Mouthereau, F., Lin, A.T.-S., Wetzel, A., Kaus, B., Willett, S., Chiang, S.-P. and Chiu, W.-Y. (2011) Sedimentology of early Pliocene sandstones in the south-western Taiwan foreland: implications for basin physiography in the early stages of collision. *J. Asian Earth Sci.*, **40**, 52–71.

Castelltort, S., Honegger, L., Adatte, T., Clark, J.D., Puigdefàbregas, C., Spangenberg, J.E., Dykstra, M.L. and Fildani, A. (2017) Detecting eustatic and tectonic signals with carbon isotopes in deep-marine strata, Eocene Ainsa Basin, Spanish Pyrenees. *Geology*, **45**, 707–710.

Cazanacli, D., Paola, C. and Parker, G. (2002) Experimental steep, braided flow: application to flooding risk on fans. *J. Hydraul. Eng.*, **128**, 322–330.

Chaisson, W.P. and Ravelo, A.C. (2000) Pliocene development of the east-west hydrographic gradient in the equatorial Pacific. *Paleoceanography*, **15**, 497–505.

Chen, P.-H. (1977) Paleomagnetic and coccolith stratigraphy of Plio-Pleistocene shallow marine sediments, Chuhuankeng, Miaoli. *Pet. Geol. Taiwan*, **14**, 219–239.

Chen, W.-S. (2016) *An Introduction to the Geology of Taiwan.* Geologic Society of Taiwan, Taipei, Taiwan.

Chen, J.-M., Li, T. and Shih, C.-F. (2010) Tropical cyclone- and monsoon-induced rainfall variability in Taiwan. *J. Climate*, **23**, 4107–4120.

Chen, C.-W., Oguchi, T., Hayakawa, Y.S., Saito, H., Chen, H., Lin, G.-W., Wei, L.-W. and Chao, Y.-C. (2018) Sediment yield during typhoon events in relation to landslides, rainfall, and catchment areas in Taiwan. *Geomorphology*, **303**, 540–548.

Chen, C.-H., Lee, C.-Y., Lin, J.-W. and Chu, M.-F. (2019) Provenance of sediments in western Foothills and Hsuehshan range (Taiwan): a new view based on the EMP monazite versus LA-ICPMS zircon geochronology of detrital grains. *Earth Sci. Rev.*, **190**, 224–246.

Chien, F.-C. and Kuo, H.-C. (2011) On the extreme rainfall of Typhoon Morakot (2009). *J. Geophys. Res.*, **116**, D05104.

Chuang, W.S. (1985) Dynamics of subtidal flow in the Taiwan strait. *J. Oceanogr. Soc. Japan*, **41**, 65–72.

**Chuang, W.-S.** (1986) A note on the driving mechanisms of current in the Taiwan Strait. *J. Oceanogr.*, **42**, 355–361.

**Clement, A.C.**, **Hall, A.** and **Broccoli, A.J.** (2004) The importance of precessional signals in the tropical climate. *Climate Dynam.*, **22**, 327–341.

**Cojan, I.** and **Gillot, T.** (2022) Paleosols in distal alluvial sequences and their formation mechanisms: Insights from a high-resolution record in a foreland basin during early Miocene (SE France). *Palaeogeogr. Palaeoclimatol. Palaeoecol.*, **595**, 110983.

**Collins, D.S.**, **Johnson, H.D.**, **Allison, P.A.**, **Guilpain, P.** and **Damit, A.R.** (2017) Coupled 'storm-flood' depositional model: application to the Miocene–Modern Baram Delta Province, north-west Borneo. *Sedimentology*, **64**, 1203–1235.

**Coumou, D.** and **Rahmstorf, S.** (2012) A decade of weather extremes. *Nat. Clim. Change*, **2**, 491–496.

**Dadson, S.J.**, **Hovius, N.**, **Chen, H.**, **Dade, W.B.**, **Hsieh, M.-L.**, **Willett, S.D.**, **Hu, J.-C.**, **Horng, M.-J.**, **Chen, M.-C.**, **Stark, C.P.**, **Lague, D.** and **Lin, J.-C.** (2003) Links between erosion, runoff variability and seismicity in the Taiwan orogen. *Nature*, **426**, 648–651.

**Dadson, S.J.**, **Hovius, N.**, **Chen, H.**, **Dade, W.B.**, **Lin, J.-C.**, **Hsu, M.-L.**, **Lin, C.-W.**, **Horng, M.-J.**, **Chen, T.-C.**, **Milliman, J.** and **Stark, C.P.** (2004) Earthquake-triggered increase in sediment delivery from an active mountain belt. *Geology*, **32**, 733.

**Dashtgard, S.E.**, **Löwemark, L.**, **Vaucher, R.**, **Pan, Y.-Y.**, **Pilarczyk, J.E.** and **Castellort, S.** (2020) Tropical cyclone deposits in the Pliocene Taiwan Strait: Processes, examples, and conceptual model. *Sediment. Geol.*, **405**, 105687.

**Dashtgard, S.E.**, **Löwemark, L.**, **Wang, P.-L.**, **Setiaji, R.A.** and **Vaucher, R.** (2021) Geochemical evidence of tropical cyclone controls on shallow-marine sedimentation (Pliocene, Taiwan). *Geology*, **49**, 566–570.

**Demenocal, P.B.** and **Rind, D.** (1993) Sensitivity of Asian and African climate to variations in seasonal insolation, glacial ice cover, sea surface temperature, and Asian orography. *J. Geophys. Res.*, **98**(D4), 7265–7287.

**Edmonds, D.A.** and **Slingerland, R.L.** (2007) Mechanics of river mouth bar formation: Implications for the morphodynamics of delta distributary networks. *J. Geophys. Res.*, **112**(F2), F02034.

**Exner, F.M.** (1925) Über die Wechselwirkung zwischen Wasser und Geschiebe in Flüssen. *Sitzungsber. Österr. Akad. Wiss., Math.-Naturwiss. Kl., Abt. II*, **134**, 165–203.

**Fedorov, A.V.**, **Brierley, C.M.** and **Emanuel, K.** (2010) Tropical cyclones and permanent El Niño in the early Pliocene epoch. *Nature*, **463**, 1066–1070.

**Filippelli, G.M.** (1997) Intensification of the Asian monsoon and a chemical weathering event in the late Miocene–early Pliocene: implications for late Neogene climate change. *Geology*, **25**, 27.

**Gai, C.**, **Liu, Q.**, **Roberts, A.P.**, **Chou, Y.**, **Zhao, X.**, **Jiang, Z.** and **Liu, J.** (2020) East Asian monsoon evolution since the late Miocene from the South China Sea. *Earth Planet. Sci. Lett.*, **530**, 115960.

**Garzanti, E.**, **Barbarano, M.**, **Andò, S.**, **Lenzi, M.**, **Deng, K.** and **Yang, S.** (2021) Provenance of Neogene sandstones in western Taiwan traced with garnet geochemistry and zircon geochronology. *Basin Res.*, **33**, 2069–2088.

**Grant, G.R.**, **Naish, T.R.**, **Dunbar, G.B.**, **Stocchi, P.**, **Kominz, M.A.**, **Kamp, P.J.J.**, **Tapia, C.A.**, **McKay, R.M.**, **Levy, R.H.** and **Patterson, M.O.** (2019) The amplitude and origin of sea-level variability during the Pliocene epoch. *Nature*, **574**, 237–241.

**Green, W.G.** and **Fearon, R.E.** (1940) Well logging by radioactivity. *Geophysics*, **5**, 272–283.

**Hajek, E.A.** and **Straub, K.M.** (2017) Autogenic sedimentation in clastic stratigraphy. *Annu. Rev. Earth Planet. Sci.*, **45**, 681–709.

**Hayes, M.O.** (1967) Hurricanes as geological agents, south Texas coast. *AAPG Bull.*, **51**, 937–942.

**Hilton, R.G.**, **Galy, A.**, **Hovius, N.**, **Horng, M.-J.** and **Chen, H.** (2010) The isotopic composition of particulate organic carbon in mountain rivers of Taiwan. *Geochim. Cosmochim. Acta*, **74**, 3164–3181.

**Horng, C.-S.** and **Shea, K.-S.** (2007) The Quaternary magnetobiostratigraphy of Taiwan and Penglai orogenic events. *Spec. Publ. Centr. Geol. Surv.*, **18**, 51–83.

**Hsieh, A.I.**, **Vaucher, R.**, **Löwemark, L.**, **Dashtgard, S.E.**, **Horng, C.-S.**, **Lin, A.T.** and **Zeeden, C.** (2023a) Influence of a rapidly uplifting orogen on the preservation of climate oscillations. *Paleoceanogr. Paleoclimatol.*, **38**, e2022PA004586.

**Hsieh, A.I.**, **Dashtgard, S.E.**, **Wang, P.-L.**, **Horng, C.-.S.**, **Su, C.-C.**, **Lin, A.T.**, **Vaucher, R.** and **Löwemark, L.** (2023b) Multi-proxy evidence for rapidly shifting sediment sources to the Taiwan Western Foreland Basin at the Miocene–Pliocene transition. *Basin Res.*, **35**, 932–948.

**Hsieh, A.I.**, **Dashtgard, S.E.**, **Clift, P.D.**, **Lo, L.**, **Vaucher, R.** and **Löwemark, L.** (2024) Competing influence of the Taiwan orogen and East Asian Summer Monsoon on South China Sea paleoenvironmental proxy records. *Palaeogeogr. Palaeoclimatol. Palaeoecol.*, **635**, 111933.

**Jerolmack, D.J.** and **Mohrig, D.** (2007) Conditions for branching in depositional rivers. *Geology*, **35**, 463–466.

**Jerolmack, D.J.** and **Paola, C.** (2010) Shredding of environmental signals by sediment transport. *Geophys. Res. Lett.*, **37**, L19401.

**Jerolmack, D.J.** and **Sadler, P.** (2007) Transience and persistence in the depositional record of continental margins. *J. Geophys. Res. Earth*, **112**, F03S13.

**Jervey, M.T.** (1988) Quantitative geological modeling of siliciclastic rock sequences and their seismic expression. In: *Sea-Level Changes: An Integrated Approach, SEPM Society for Sedimentary Geology* (Ed Wilgus, C.K.), Vol. **42**, pp. 47–49.

**Jian, Z.**, **Yu, Y.**, **Li, B.**, **Wang, J.**, **Zhang, X.** and **Zhou, Z.** (2006) Phased evolution of the south–north hydrographic gradient in the South China Sea since the middle Miocene. *Palaeogeogr. Palaeoclimatol. Palaeoecol.*, **230**, 251–263.

**Kaboth-Bar, S.** and **Mudelsee, M.** (2022) The multifaceted history of the Walker Circulation during the Plio-Pleistocene. *Qua. Sci. Rev.*, **286**, 107529.

**Kao, S.J.** and **Milliman, J.D.** (2008) Water and sediment discharge from small mountainous rivers, Taiwan: the roles of lithology, episodic events, and human activities. *J. Geol.*, **116**, 431–448.

**Kao, S.J.**, **Hilton, R.G.**, **Selvaraj, K.**, **Dai, M.**, **Zehetner, F.**, **Huang, J.C.**, **Hsu, S.C.**, **Sparkes, R.**, **Liu, J.T.**, **Lee, T.Y.**, **Yang, J.Y.T.**, **Galy, A.**, **Xu, X.** and **Hovius, N.** (2014) Preservation of terrestrial organic carbon in marine sediments offshore Taiwan: mountain building and atmospheric carbon dioxide sequestration. *Earth Surf. Dyn.*, **2**, 127–139.

**Kelman, I.** (2013) Saffir–Simpson hurricane intensity scale. In: *Encyclopedia of Natural Hazards* (Ed Bobrowsky, P.T.), pp. 882–883. Springer, Dordrecht.

**Kim, W.** and **Paola, C.** (2007) Long-period cyclic sedimentation with constant tectonic forcing in an experimental relay ramp. *Geology*, **35**, 331–334.

**Kossin, J.P.**, **Knapp, K.R.**, **Olander, T.L.** and **Velden, C.S.** (2020) Global increase in major tropical cyclone exceedance probability over the past four decades. *Proc. Natl. Acad. Sci.*, **117**, 11975–11980.

**Laskar, J.**, **Robutel, P.**, **Joutel, F.**, **Gastineau, M.**, **Correia, A.C.M.** and **Levrard, B.** (2004) A long-term numerical solution for the insolation quantities of the earth. *Astron. Astrophys.*, **428**, 261–285.

**Lazarus, E.D.**, **Harley, M.D.**, **Blenkinsopp, C.E.** and **Turner, I.L.** (2019) Environmental signal shredding on sandy coastlines. *Earth Surf. Dyn.*, **7**, 77–86.

**Lee, T.-Y.**, **Huang, J.-C.**, **Lee, J.-Y.**, **Jien, S.-H.**, **Zehetner, F.** and **Kao, S.-J.** (2015) Magnified sediment export of small mountainous rivers in Taiwan: Chain reactions from increased rainfall intensity under global warming. *PLoS One*, **10**, e0138283.

**Li, B.**, **Wang, J.**, **Huang, B.**, **Li, Q.**, **Jian, Z.**, **Zhao, Q.**, **Su, X.** and **Wang, P.** (2004) South China Sea surface water evolution over the last 12 Myr: a south-north comparison from Ocean Drilling Program Sites 1143 and 1146. *Paleoceanography*, **19**, PA1009.

**Li, L.**, **Li, Q.**, **Tian, J.**, **Wang, P.**, **Wang, H.** and **Liu, Z.** (2011) A 4-Ma record of thermal evolution in the tropical western Pacific and its implications on climate change. *Earth Planet. Sci. Lett.*, **309**, 10–20.

**Li, Q.**, **Gasparini, N.M.** and **Straub, K.M.** (2018) Some signals are not the same as they appear: how do erosional landscapes transform tectonic history into sediment flux records? *Geology*, **46**, 407–410.

**Lin, W.** and **Bhattacharya, J.P.** (2021) Storm-flood-dominated delta: A new type of delta in stormy oceans. *Sedimentology*, **68**, 1109–1136.

**Lin, C.-W.** and **Chen, W.-S.** (2016) *Geologic Map of Taiwan*. Geological Society of Taiwan, Taipei, Taiwan.

**Lin, A.T.-S.** and **Watts, A.B.** (2002) Origin of the West Taiwan basin by orogenic loading and flexure of a rifted continental margin. *J. Geophys. Res. Solid Earth*, **107**(B9), ETG 2-1-ETG 2-19.

**Lin, A.T.-S.**, **Watts, A.B.** and **Hesselbo, S.P.** (2003) Cenozoic stratigraphy and subsidence history of the South China Sea margin in the Taiwan region. *Basin Res.*, **15**, 453–478.

**Lin, S.F.**, **Tang, T.Y.**, **Jan, S.** and **Chen, C.J.** (2005) Taiwan strait current in winter. *Cont. Shelf Res.*, **25**, 1023–1042.

**Lin, A.T.-S.**, **Wang, S.-M.**, **Hung, J.-H.**, **Wu, M.-S.** and **Liu, C.-S.** (2007) Lithostratigraphy of the Taiwan Chelungpu-Fault Drilling Project—a borehole and its neighboring region, Central Taiwan. *Terrestr. Atmos. Ocean. Sci.*, **18**, 223.

**Lin, B.**, **Liu, Z.**, **Eglinton, T.I.**, **Kandasamy, S.**, **Blattmann, T.M.**, **Haghipour, N.**, **Huang, K.-F.** and **You, C.-F.** (2020) Island-wide variation in provenance of riverine sedimentary organic carbon: a case study from Taiwan. *Earth Planet. Sci. Lett.*, **539**, 116238.

**Liu, Y.**, **Lo, L.**, **Shi, Z.**, **Wei, K.Y.**, **Chou, C.J.**, **Chen, Y.C.**, **Chuang, C.K.**, **Wu, C.C.**, **Mii, H.S.**, **Peng, Z.**, **Amakawa, H.**, **Burr, G.S.**, **Lee, S.Y.**, **DeLong, K.L.**, **Elderfield, H.** and **Shen, C.C.** (2015) Obliquity pacing of the western Pacific Intertropical Convergence Zone over the past 282,000 years. *Nat. Commun.*, **6**, 10018.

**Liu, C.**, **Clift, P.D.**, **Giosan, L.**, **Miao, Y.**, **Warny, S.** and **Wan, S.** (2019) Paleoclimatic evolution of the SW and NE South China Sea and its relationship with spectral reflectance data over various age scales. *Palaeogeogr. Palaeoclimatol. Palaeoecol.*, **525**, 25–43.

**Lourens, L.J.**, **Antonarakou, A.**, **Hilgen, F.J.**, **van Hoof, A.A.M.**, **Vergnaud-Grazzini, C.** and **Zachariasse, W.J.** (1996) Evaluation of the Plio-Pleistocene astronomical timescale. *Paleoceanogr. Paleoclimatol.*, **11**, 391–413.

**MacEachern, J.A.** and **Bann, K.L.** (2020) The *Phycosiphon* ichnofacies and the *Rosselia* ichnofacies: two new ichnofacies for marine deltaic environments. *J. Sediment. Res.*, **90**, 855–886.

**MacEachern, J.A.** and **Bann, K.L.** (2023) Departures from the archetypal deltaic ichnofacies. *Art Ther.*, **522**, 175–213.

**MacEachern, J.A.**, **Bann, K.L.**, **Bhattacharya, J.P.** and **Howell, C.D.** (2005) Ichnology of deltas: organism responses to the dynamic interplay of rivers, waves, storms, and tides. In: *River Deltas–Concepts, Models, and Examples*, SEPM Special Publication, Vol. **83**, pp. 49–85.

**MacEachern, J.A.**, **Pemberton, S.G.**, **Bann, K.L.** and **Gingras, M.K.** (2007) Departures from the archetypal ichnofacies: effective recognition of physico-chemical stresses in the rock record. In: *Applied Ichnology*, SEPM Short Course Notes (Ed MacEachern, J.A.), Vol. **52**, pp. 65–93.

**Marshall, N.**, **Zeeden, C.**, **Hilgen, F.** and **Krijgsman, W.** (2017) Milankovitch cycles in an equatorial delta from the Miocene of Borneo. *Earth Planet. Sci. Lett.*, **472**, 229–240.

**Meyers, S.R.** (2014) Astrochron: An R Package for Astrochronology.

**Miller, K.G.**, **Browning, J.V.**, **Schmelz, W.J.**, **Kopp, R.E.**, **Mountain, G.S.** and **Wright, J.D.** (2020) Cenozoic sea-level and cryospheric evolution from deep-sea geochemical and continental margin records. *Sci. Adv.*, **6**, eaaz1346.

**Milliman, J.D.** and **Kao, S.-J.** (2005) Hyperpycnal discharge of fluvial sediment to the ocean: Impact of super-typhoon Herb (1996) on Taiwanese rivers. *J. Geol.*, **113**, 503–516.

**Milliman, J.D.**, **Lin, S.W.**, **Kao, S.J.**, **Liu, J.P.**, **Liu, C.S.**, **Chiu, J.K.** and **Lin, Y.C.** (2007) Short-term changes in seafloor character due to flood-derived hyperpycnal discharge: Typhoon Mindulle, Taiwan, July 2004. *Geology*, **35**, 779–782.

**Milliman, J.D.**, **Lee, T.Y.**, **Huang, J.C.** and **Kao, S.J.** (2017) Impact of catastrophic events on small mountainous rivers: Temporal and spatial variations in suspended- and dissolved-solid fluxes along the Choshui River, central western Taiwan, during typhoon Mindulle, July 2–6, 2004. *Geochim. Cosmochim. Acta*, **205**, 272–294.

**Mills, P.C.** (1983) Genesis and diagnostic value of soft-sediment deformation structures—A review. *Sediment. Geol.*, **35**, 83–104.

**Mitchell, D.A.**, **Teague, W.J.**, **Jarosz, E.** and **Wang, D.W.** (2005) Observed currents over the outer continental shelf during Hurricane Ivan. *Geophys. Res. Lett.*, **32**, L11610.

**Myrow, P.M.** and **Southard, J.B.** (1996) Tempestite deposition. *J. Sediment. Res.*, **66**, 875–887.

**Myrow, P.M.**, **Fischer, W.** and **Goodge, J.W.** (2002) Wave-modified turbidites: combined-flow shoreline and shelf deposits, Cambrian, Antarctica. *J. Sediment. Res.*, **72**, 641–656.

**Nagel, S.**, **Castelltort, S.**, **Wetzel, A.**, **Willett, S.D.**, **Mouthereau, F.** and **Lin, A.T.** (2013) Sedimentology and foreland basin paleogeography during Taiwan arc continent collision. *J. Asian Earth Sci.*, **62**, 180–204.

**Owen, G.**, **Moretti, M.** and **Alfaro, P.** (2011) Recognising triggers for soft-sediment deformation: current understanding and future directions. *Sediment. Geol.*, **235**, 133–140.

**Pan, T.-Y.**, **Lin, A.T.-S.** and **Chi, W.-R.** (2015) Paleoenvironments of the evolving Pliocene to early Pleistocene foreland basin in northwestern Taiwan: an example from the Dahan River section. *Island Arc.*, **24**, 317–341.

**Prell, W.L.** and **Kutzbach, J.E.** (1987) Monsoon variability over the past 150,000 years. *J. Geophys. Res.*, **92**(D7), 8411–8425.

**Prell, W.L.** and **Kutzbach, J.E.** (1992) Sensitivity of the Indian monsoon to forcing parameters and implications for its evolution. *Nature*, **360**, 352–647.

**Prieur, M.**, **Robin, C.**, **Braun, J.**, **Vaucher, R.**, **Whittaker, A.C.**, **Jaimes-Gutierrez, R.**, **Wild, A.**, **McLeod, J.S.**, **Malatesta, L.**, **Fillon, C.**, **Schlunegger, F.**, **Sømme, T.O.** and **Castelltort, S.** (2025) Climate control on erosion: evolution of sediment flux from mountainous catchments during a global warming event, PETM, Southern Pyrenees, Spain. *Geophys. Res. Lett.*, **52**, e2024GL112404.

**Qu, T.** (2000) Upper-layer circulation in the South China Sea. *J. Phys. Oceanogr.*, **30**, 1450–1460.

**Qu, T.**, **Girton, J.B.** and **Whitehead, J.A.** (2006) Deepwater overflow through Luzon Strait. *J. Geophys. Res.*, **111**, C01002.

**R Core Team** (2022) *R: A Language and Environment for Statistical Computing*. R Foundation for Statistical Computing, Vienna, Austria.

**Reineck, H.-E.** (1963) Sedimentgefüge im Bereich der südlichen Nordsee. *Abh. Senckenberg. Naturforsch. Ges.*, **505**, 1–138.

**Romans, B.W.**, **Castelltort, S.**, **Covault, J.A.**, **Fildani, A.** and **Walsh, J.P.** (2016) Environmental signal propagation in sedimentary systems across timescales. *Earth Sci. Rev.*, **153**, 7–29.

**Sadler, P.M.** (1981) Sediment accumulation rates and the completeness of stratigraphic sections. *J. Geol.*, **89**, 569–584.

**Schlager, W.** (1993) Accommodation and supply—a dual control on stratigraphic sequences. *Sediment. Geol.*, **86**, 111–136.

**Schlumberger, G.** (1989) *Log Interpretation Principles/Applications*, p. 233. Schlumberger, Houston.

**Shanmugam, G.** (2017) Global case studies of soft-sediment deformation structures (SSDS): definitions, classifications, advances, origins, and problems. *J. Palaeogeogr.*, **6**, 251–320.

**Sharman, G.R.**, **Sylvester, Z.** and **Covault, J.A.** (2019) Conversion of tectonic and climatic forcings into records of sediment supply and provenance. *Sci. Rep.*, **9**, 4115.

**Simoes, M.** and **Avouac, J.P.** (2006) Investigating the kinematics of mountain building in Taiwan from the spatiotemporal evolution of the foreland basin and western foothills. *J. Geophys. Res.*, **111**(B10), B10401.

**Sun, T.** and **Parker, G.** (2005) Transportational cyclic steps created by flow over an erodible bed. Part 2. Theory and numerical simulation. *J. Hydraul. Res.*, **43**, 502–514.

**Sun, Y.**, **An, Z.**, **Clemens, S.C.**, **Bloemendal, J.** and **Vandenberghe, J.** (2010) Seven million years of wind and precipitation variability on the Chinese Loess Plateau. *Earth Planet. Sci. Lett.*, **297**, 525–535.

**Suppe, J.** (1981) Mechanics of mountain building and metamorphism in Taiwan. *Mem. Geol. Soc. China*, **4**, 67–89.

**Suppe, J.** (1984) Kinematics of arc-continent collision, flipping of subduction and back-arc spreading near Taiwan. *Mem. Geol. Soc. China*, **4**, 67–89.

**Tachikawa, K.**, **Cartapanis, O.**, **Vidal, L.**, **Beaufort, L.**, **Barlyaeva, T.** and **Bard, E.** (2011) The precession phase of hydrological variability in the Western Pacific Warm Pool during the past 400 ka. *Quat. Sci. Rev.*, **30**, 3716–3727.

**Taner, M.T.** (1992) *Attributes Revisited (Technical Report)*. Rock Solid Images Inc, Houston, Texas.

**Taylor, A.M.** and **Goldring, R.** (1993) Description and analysis of bioturbation and ichnofabric. *J. Geol. Soc. Lond.*, **150**, 141–148.

**Teague, W.J.**, **Jarosz, E.**, **Wang, D.W.** and **Mitchell, D.A.** (2007) Observed oceanic response over the upper continental slope and outer shelf during Hurricane Ivan. *J. Phys. Oceanogr.*, **37**, 2181–2206.

**Teng, L.S.** (1990) Geotectonic evolution of late Cenozoic arc-continent collision in Taiwan. *Tectonophysics*, **183**, 57–76.

**Teng, L.S.**, **Hsiehz, Y.W.**, **Tanghz, C.H.**, **Huangghz, C.Y.**, **Huang, T.C.** and **Yuuang, M.S.** (1991) Tectonic aspects of the Paleogene depositional basin of northern Taiwan. *Proc. Geol. Soc. China*, **34**, 313–336.

**Tian, J.**, **Pak, D.K.**, **Wang, P.**, **Lea, D.**, **Cheng, X.** and **Zhao, Q.** (2006) Late Pliocene monsoon linkage in the tropical South China Sea. *Earth Planet. Sci. Lett.*, **252**, 72–81.

**Tiedemann, R.**, **Sarnthein, M.** and **Shackleton, N.J.** (1994) Astronomic timescale for the Pliocene Atlantic $\delta^{18}O$ and dust flux records of Ocean Drilling Program Site 659. *Paleoceanogr. Paleoclimatol.*, **9**, 619–638.

**Vaucher, R.** and **Dashtgard, S.E.** (2022) Nearshore bedforms. In: *Treatise on Geomorphology* (Ed Shroder, J.J.F.), pp. 230–246. Academic Press, Elsevier.

**Vaucher, R.**, **Dashtgard, S.E.**, **Horng, C.S.**, **Zeeden, C.**, **Dillinger, A.**, **Pan, Y.Y.**, **Setiaji, R.A.**, **Chi, W.R.** and **Löwemark, L.** (2021) Insolation-paced sea level and sediment flux during the early Pleistocene in Southeast Asia. *Sci. Rep.*, **11**, 16707.

**Vaucher, R.**, **Dillinger, A.**, **Hsieh, A.I.**, **Chi, W.R.**, **Löwemark, L.** and **Dashtgard, S.E.** (2023a) Storm-flood-dominated delta succession in the Pleistocene Taiwan Strait. *Deposit. Rec.*, **9**, 1–24.

**Vaucher, R.**, **Zeeden, C.**, **Hsieh, A.I.**, **Kaboth-Bahr, S.**, **Lin, A.T.**, **Horng, C.-S.** and **Dashtgard, S.E.** (2023b) Hydroclimate dynamics during the Plio-Pleistocene transition in the northwest Pacific realm. *Global Planet. Change*, **223**, 104088.

**Vaucher, R.**, **Musajo, C.**, **Spangenberg, J.E.**, **Poyatos-Moré, M.**, **Zeeden, C.**, **Puigdefàbregas, C.**, **Prieur, M.**, **Castelltort, S.** and **Adatte, T.** (2024) Sediment supply variation control on Lower Eocene delta sequences (Tremp Basin, Spain). *Geology*, **53**, 83–88.

**Wan, S.**, **Li, A.**, **Clift, P.D.** and **Jiang, H.** (2006) Development of the East Asian summer monsoon: Evidence from the sediment record in the South China Sea since 8.5 Ma. *Palaeogeogr. Palaeoclimatol. Palaeoecol.*, **241**, 139–159.

**Wan, S.**, **Tian, J.**, **Steinke, S.**, **Li, A.** and **Li, T.** (2010) Evolution and variability of the East Asian summer monsoon during the Pliocene: evidence from clay mineral records of the South China Sea. *Palaeogeogr. Palaeoclimatol. Palaeoecol.*, **293**, 237–247.

**Wang, Y.H.**, **Jan, S.** and **Wang, D.P.** (2003) Transports and tidal current estimates in the Taiwan Strait from shipboard ADCP observations (1999–2001). *Estuar. Coast. Shelf Sci.*, **57**, 193–199.

**Wang, L.**, **Pawlowicz, R.**, **Wu, X.** and **Yue, X.** (2021) Wintertime variability of currents in the Southwestern Taiwan Strait. *J. Geophys. Res. Oceans*, **126**, e2020JC016586.

**Whittaker, A.C.**, **Duller, R.A.**, **Springett, J.**, **Smithells, R.A.**, **Whitchurch, A.L.** and **Allen, P.A.** (2011) Decoding downstream trends in stratigraphic grain size as a function of tectonic subsidence and sediment supply. *Geol. Soc. Am. Bull.*, **123**, 1363–1382.

**Wilkens, R.H.**, **Westerhold, T.**, **Drury, A.J.**, **Lyle, M.**, **Gorgas, T.** and **Tian, J.** (2017) Revisiting the Ceara Rise, equatorial Atlantic Ocean: isotope stratigraphy of ODP Leg 154 from 0 to 5 Ma. *Clim. Past*, **13**, 779–793.

**Wu, L.**, **Liang, J.** and **Wu, C.-C.** (2011) Monsoonal influence on Typhoon Morakot (2009). Part I: observational analysis. *J. Atmos. Sci.*, **68**, 2208–2221.

**Yan, Q.**, **Wei, T.**, **Korty, R.L.**, **Kossin, J.P.**, **Zhang, Z.** and **Wang, H.** (2016) Enhanced intensity of global tropical cyclones during the mid-Pliocene warm period. *Proc. Natl. Acad. Sci.*, **113**, 12963–12967.

**Yan, Q.**, **Wei, T.**, **Zhang, Z.** and **Jiang, N.** (2019) Orbitally induced variation of tropical cyclone genesis potential over the western North Pacific during the mid-Piacenzian Warm Period: a modeling perspective. *Paleoceanogr. Paleoclimatol.*, **34**, 902–916.

**Yin, S.**, **Hernández-Molina, F.J.**, **Lin, L.**, **Chen, J.**, **Ding, W.** and **Li, J.** (2021) Isolation of the South China Sea from the North Pacific Subtropical Gyre since the latest Miocene due to formation of the Luzon Strait. *Sci. Rep.*, **11**, 1562.

**Yin, S.**, **Hernández-Molina, F.J.**, **Lin, L.**, **He, M.**, **Gao, J.** and **Li, J.** (2023) Plate convergence controls long-term full-depth circulation of the South China Sea. *Mar. Geol.*, **459**, 107050.

**Zeeden, C.**, **Kaboth, S.**, **Hilgen, F.J.** and **Laskar, J.** (2018) Taner filter settings and automatic correlation optimisation for cyclostratigraphic studies. *Comput. Geosci.*, **119**, 18–28.

**Zhang, Y.G.**, **Ji, J.**, **Balsam, W.**, **Liu, L.** and **Chen, J.** (2009) Mid-Pliocene Asian monsoon intensification and the onset of Northern Hemisphere glaciation. *Geology*, **37**, 599–602.

**Zhang, Y.**, **Zhang, Z.**, **Chen, D.**, **Qiu, B.** and **Wang, W.** (2020) Strengthening of the Kuroshio current by intensifying tropical cyclones. *Science*, **368**, 988–993.

**Zhang, R.**, **Li, X.**, **Xu, Y.**, **Li, J.**, **Sun, L.**, **Yue, L.**, **Pan, F.**, **Xian, F.**, **Wei, X.** and **Cao, Y.** (2022) The 173-kyr obliquity cycle pacing the Asian Monsoon in the Eastern Chinese Loess Plateau from Late Miocene to Pliocene. *Geophys. Res. Lett.*, **49**, e2021GL097008.

## Supporting Information

Additional information may be found in the online version of this article:

**Fig. S1.** Outcrop and facies logs of the Kueichulin Fm outcrop along the Da'an River in the depth domain (A) compared to facies (B) and sedimentary data (C) tied to magnetobiostratigraphic age boundaries from Hsieh et al. (2023). The p-0.5 t curve (D) is the mix-standardized precession minus 0.5 times standardized obliquity, which represents ~65° N insolation (Laskar *et al.*, 2004). Astronomical solutions for the Earth's obliquity, eccentricity and precession for the studied time interval are from Laskar *et al.* (2004) (E) and are used for comparison with the sedimentary record. Global mean sea-level is from Miller *et al.* (2020) (F). Dash-dot lines indicate boundaries between major shifts in depositional settings interpreted from facies. White intervals in the facies log denote inaccessible, covered or collapsed outcrop sections. Acronyms: [grain size] mud (m); very fine grained (vf); fine grained (f), medium grained (m) | [ichnology] bioturbation index (BI) | [lithology] mudstone (mst); silty to sandy mudstone (sl–s mst); muddy to silty sandstone (m–sl sst); sandstone (sst).

**Fig. S2.** Core and facies logs of the cored interval through the Kueichulin Fm at TCDP-A in the depth domain (A) compared to facies (B), and sedimentary data and gamma-ray profile (C) tied to magnetobiostratigraphic age boundaries from Hsieh *et al.* (2023b). The p-0.5 t curve (D) is the mix-standardized precession minus 0.5 times of standardized obliquity, which represents ~65° N insolation (Laskar *et al.*, 2004). Astronomical solutions for the Earth's obliquity, eccentricity and precession for the studied time interval are from Laskar *et al.* (2004) (E) and are used for comparison with the sedimentary record. Global mean sea-level is from Miller *et al.* (2020) (F). Dash-dot lines indicate boundaries between major shifts in depositional settings interpreted from facies. White intervals in the facies log denote missing core. Acronyms: [grain size] mud (m); very fine grained (vf); fine grained (f), medium grained (m) | [ichnology] bioturbation index (BI) | [lithology] mudstone (mst); silty to sandy mudstone (sl–s mst); muddy to silty sandstone (m–sl sst); sandstone (sst).

**Fig. S3A.** Tuned facies data for the Da'an River outcrop filtered using the Taner bandpass filter for short eccentricity (100 Kyr periodicity), precession (20 Kyr periodicity) and obliquity (41 Kyr periodicity). The pink dashed lines represent the amplitude (i.e. strength) of orbital signals preserved in the record after applying the bandpass filter. The orange line represents the upper envelope of the filtered signal, which highlights peaks that correspond to strong orbital signals preserved in the record. Astronomical solution of the Earth's eccentricity, precession and obliquity indices for the studied time interval is from Laskar *et al.* (2004).

**Fig. S3B.** Tuned lithology data for the Da'an River outcrop filtered using the Taner bandpass filter for short eccentricity (100 Kyr periodicity), precession (20 Kyr periodicity) and obliquity (41 Kyr periodicity). The pink dashed lines represent the amplitude (i.e. strength) of orbital signals preserved in the record after applying the bandpass filter. The orange line represents the upper envelope of the filtered signal, which highlights peaks that correspond to strong orbital signals preserved in the record. Astronomical solution of the Earth's eccentricity, precession and obliquity indices for the studied time interval is from Laskar *et al.* (2004).

**Fig. S3C.** Tuned grain-size data for the Da'an River outcrop filtered using the Taner bandpass filter for short eccentricity (100 Kyr periodicity), precession (20 Kyr periodicity) and obliquity (41 Kyr periodicity). The pink dashed lines represent the amplitude (i.e. strength) of orbital signals preserved in the record after applying the bandpass filter. The orange line represents the upper envelope of the filtered signal, which highlights peaks that correspond to strong orbital signals preserved in the record. Astronomical solution of the Earth's eccentricity, precession and obliquity indices for the studied time interval are from Laskar *et al.* (2004).

**Fig. S3D.** Tuned bioturbation index data for the Da'an River outcrop filtered using the Taner bandpass filter for short eccentricity (100 Kyr periodicity), precession (20 Kyr periodicity) and obliquity (41 Kyr periodicity). The pink dashed lines represent the amplitude (i.e. strength) of orbital signals preserved in the record after applying the bandpass filter. The orange line represents the upper envelope of the filtered signal, which highlights peaks that correspond to strong orbital signals preserved in the record. Astronomical solution of the Earth's eccentricity, precession and obliquity indices for the studied time interval are from Laskar *et al.* (2004).

**Fig. S4A.** Tuned facies data for TCDP-A filtered using the Taner bandpass filter for short eccentricity (100 Kyr periodicity), precession (20 Kyr periodicity) and obliquity (41 Kyr periodicity). The pink dashed lines represent the amplitude (i.e. strength) of orbital signals preserved in the record after applying the bandpass filter. The orange line represents the upper envelope of the filtered signal, which highlights peaks that correspond to strong orbital signals preserved in the record. Astronomical solution of the Earth's eccentricity, precession and obliquity indices for the studied time interval are from Laskar *et al.* (2004).

**Fig. S4B.** Tuned lithology data for TCDP-A filtered using the Taner bandpass filter for short eccentricity (100 Kyr periodicity), precession (20 Kyr periodicity) and obliquity (41 Kyr periodicity). The pink dashed lines represent the amplitude (i.e. strength) of orbital signals preserved in the record after applying the bandpass filter. The orange line represents the upper envelope of the filtered signal, which highlights peaks that correspond to strong orbital signals preserved in the record. Astronomical solution of the Earth's eccentricity, precession and obliquity indices for the studied time interval are from Laskar *et al.* (2004).

**Fig. S4C.** Tuned gamma-ray data for TCDP-A filtered using the Taner bandpass filter for short eccentricity (100 Kyr periodicity), precession (20 Kyr periodicity) and obliquity (41 Kyr periodicity). The pink dashed lines represent the amplitude (i.e. strength) of orbital signals preserved in the record after applying the bandpass filter. The orange line represents the upper envelope of the filtered signal, which highlights peaks that correspond to strong orbital signals preserved in the record. Astronomical solution of the Earth's eccentricity, precession and obliquity indices for the studied time interval is from Laskar *et al.* (2004).

**Fig. S4D.** Tuned bioturbation index data for TCDP-A filtered using the Taner bandpass filter for short eccentricity (100 Kyr periodicity), precession (20 Kyr periodicity) and obliquity (41 Kyr periodicity). The pink dashed lines represent the amplitude (i.e. strength) of orbital signals preserved in the record after applying the bandpass filter. The orange line represents the upper envelope of the filtered signal, which highlights peaks that correspond to strong orbital signals preserved in the record. Astronomical solution of the Earth's eccentricity, precession and obliquity indices for the studied time interval are from Laskar *et al.* (2004).